A&A 378, 861–882 (2001)
DOI: 10.1051/0004-6361:20011202

Astronomy & Astrophysics

High and intermediate-resolution spectroscopy of Be stars⋆,⋆⋆

An atlas of Hγ, He I 4471 and Mg II 4481 lines

J. Chauville[1], J. Zorec[2], D. Ballereau[1], N. Morrell[3], L. Cidale[3,⋆⋆⋆], and A. Garcia[2]

[1] DASGAL, UMR 8633 du CNRS, Observatoire de Paris-Meudon, 92195 Meudon, France
[2] Institut d'Astrophysique de Paris, CNRS, 98bis Bld. Arago, 75014 Paris, France
[3] Facultad de Ciencias Astronómicas y Geofísicas, Universidad de La Plata, Paseo del Bosque S/N, 1900 La Plata, Argentina

Received 19 June 2001 / Accepted 16 August 2001

Abstract. We present an atlas of Hγ, He I λ 4471 and Mg II λ 4481 line profiles obtained in a 10 year observation period of 116 Be stars, which enabled many of them to be observed at quite different emission epochs. From the best fit of the observed He I λ 4471 line profiles with non-LTE, uniform ($T_{\rm eff}, \log g$) and full limb-darkened model line profiles, we determined the $V \sin i$ of the program stars. To account, to some degree, for the line formation peculiarities related to the rapid rotation-induced non-uniform distributions of temperature and gravity on the stellar surface, the fit was achieved by considering ($T_{\rm eff}, \log g$) as free parameters. This method produced $V \sin i$ estimations that correlate with the rotational velocities determined by Slettebak (1982) within a dispersion $\sigma \leq$ 30 km s^{-1} and without any systematic deviation. They can be considered as given in the new Slettebak's et al. (1975) system. Only 13 program stars have discrepant $V \sin i$ values. In some objects, this discrepancy could be attributed to binary effects. Using the newly determined $V \sin i$ parameters, we found that the ratio of true rotational velocities $V/V_{\rm c}$ of the program Be stars has a very low dispersion around the mean value. Assuming then that all the stars are rigid rotators with the same ratio $V(\overline{\omega})/V_{\rm c}$, we looked for the value of $\overline{\omega}$ that better represents the distribution of $V \sin i/V_{\rm c}$ for randomly oriented rotational axes. We obtained $\overline{\omega} = 0.795$. This value enabled us to determine the probable inclination angle of the stellar rotation axis of the program stars. In the observed line profiles of Hγ, He I λ 4471, Mg II λ 4481 and Fe II λ 4351 we measured several parameters related to the absorption and/or emission components, such as: equivalent width, residual emission and/or absorption intensity, FWHM, emission peak separations, etc. The parameters related to the Hγ line emission profiles were used to investigate the structure of the nearby environment of the central star. From the characteristics of the correlations between these quantities and the inferred inclination angle, we concluded that in most of cases the Hγ line emission forming regions may not be strongly flattened. Using a simple representation of the radiation flux emitted by the star+envelope system, we derived first order estimates of physical parameters characterizing the Hγ line emission formation region. Thus, we obtained that the total extent of the Hγ region is $R_{\rm f} \simeq 2.5 \pm 1.0\ R_*$ and that the density distribution in these layers can be mimicked with a power law $\rho \sim R^{-\alpha}$, where $\alpha = 2.5^{+2.2}_{-0.6}$. The same approach enabled us to estimate the optical depth of the Hγ line emission formation region. From its dependence with the aspect angle, we concluded that these regions are caracterized by a modest flattening and that the ρ(equator)/ρ(pole) density contrast of the circumstellar envelope near the star should be two orders of magnitude lower than predicted by models based on a priori disc-shaped circumstellar envelopes. We found that the separation between the emission peaks, $\Delta_{\rm p}$, and the full width at half maximum, $\Delta_{1/2}$, of the Hγ line emission are not only sensitive to kinematic effects, but to line optical depth as well. This finding agrees with previous theoretical predictions and confirms that Huang's (1972) relation overestimates the extent of the Hγ line emission formation region.

Key words. stars: emission-line, Be – stars: fundamental parameters – techniques: spectroscopic – line: profiles

Send offprint requests to: J. Zorec, e-mail: zorec@iap.fr

⋆ Data obtained at CASLEO operated under agreement between the CONICET and the National Universities of La Plata, Córdoba and San Juan, Argentina, at ESO La Silla, Chile and at OHP, France.

⋆⋆ Tables 2 to 7 and Figs. 1 and 2 are only available in full in electronic form at CDS via anonymous ftp to cdsarc.u-strasbg.fr (130.79.128.5) or via http://cdsweb.u-strasbg.fr/cgi-bin/qcat?J/A+A/378/861

⋆⋆⋆ LC and NM Members of the Carrera del Investigador Científico, CONICET, Argentina.

1. Introduction

The definition of Be stars (Jaschek et al. 1981) as non-supergiant B stars which at least once have shown some emission in the Balmer lines implies a vast phenomenology whose characteristics, the evolution of their understanding and the questions which still remain open have been widely reviewed in the last five IAU colloquia and symposia on these stars (Slettebak 1976; Jaschek & Groth 1982; Slettebak & Snow 1987; Balona et al. 1994; Smith et al. 2000). The outstanding physical problems related to them can roughly be summarized into two groups of global questions: a) what is the nature of the central stars and when does the Be phenomenon occur during their evolutionary span?; b) what is the structure of their circumstellar envelopes (CE) and how are they produced? To tackle the first question we need to know the fundamental parameters of these objects. Among these parameters, those relating to stellar rotation, in particular the $V \sin i$, are of primary significance. Nevertheless, rare are those Be stars which have spectral signatures from their photospheres that are unaffected by circumstellar and/or exophotospheric activities. Thus, the determination of fundamental parameters, in particular the $V \sin i$ of Be stars, is subject to considerable uncertainty. Moreover, as Be stars are fast rotators, their temperature and gravity are aspect angle-dependent and do not have the straightforward meaning they have in slow rotators. The existing $V \sin i$ of Be stars were determined using not only different measurement techniques but, for each star, the observations were made either only once or at only a single emission/absorption-variation phase (cf. Uesugi & Fukuda's 1982, compilation; Slettebak 1982; Halbedel 1996; Brown & Verschueren 1997; Steele et al. 1999). Apart from the systematic deviations which arise because of differences in the characteristics of the several methods used, a non-negligible number of Be stars still show a large scatter of their $V \sin i$ estimates, which are probably due to the stellar and circumstellar activities and whose strengths depend on the epoch of observation. The He I 4471 line of the triplet series (Ballereau et al. 1995) is among the spectral lines expected to be less affected by the emissions and/or absorptions produced by the CE, so that it could be assumed to be a reliable signature of the stellar photosphere. However, depending on the star and on the epoch of observation, the photospheric He I 4471 absorption line may still be affected by the veiling effect due to the flux excess produced in the CE. The intensity of the CE continuum radiation is correlated with the emission intensity observed in the Hγ line and their correlation is rather well defined (Ballereau et al. 1995; Zorec et al. 1996), because the emission in the Hγ line and in the continuum are both formed in more or less the same layers of the CE. On average, these layers are closer to the central star than those where the otherwise stronger emissions observed in the Hβ and Hα lines are formed. The fact that these emissions arise in layers which are close to the central star might help us to gather new information on the characteristics of CE near the star: geometry (flat discs or equivalent to ellipsoidal distributions of gas entirely covering the central star), emissivity (optical depths, temperature), dynamics (velocity fields, density distribution). To this purpose, we have undertaken a long-term observation of a spectral region around the He I 4471 transition as simultaneously as possible with the Hγ line for 116 Be stars.

The aim of the present paper can then be summarized as: 1) to publish the atlas of all Hγ, He I 4471 and the neighbouring Mg II 4481 line profiles of 116 Be stars that we have obtained during the last 10 years, many of them observed several times and at different epochs; 2) to give a new estimate of their $V \sin i$ parameter derived by taking into account as much as possible the systematic effects related to the specific characteristics of Be stars; 3) to give the measurements that were carried out on the line profiles presented in the atlas; 4) to present some preliminary insights and discussions arising from the information in the data obtained.

2. Observations

2.1. Data acquisition

We present high and intermediate-resolution Hγ, He I 4471 and Mg II 4481 line profiles of 116 Be stars observed in three Observatories, Complejo Astronómico El Leoncito (CASLEO), Argentina ($\phi = -31°47'57''$, $\lambda = 4^{\rm h}37^{\rm m}12^{\rm s}$ and 2550-m altitude), ESO-La Silla (Chile) and OHP (France).

For the spectra obtained at CASLEO we used the 2.15-m telescope, a twin of the similarly sized telescope at KPNO and a REOSC échelle spectrograph, which is on loan from the Institut d'Astrophysique de Liège, Belgium, and a Tek 1024 × 1024 CCD. A 400 lines mm^{-1} grating was used as cross disperser. We used two different grating tilts in order to cover the blue and red regions of the spectrum, respectively. For the "blue" set-up, we used an angle of 6°50′, resulting in a wavelength coverage from about λ3900 to λ6400 Å at a reciprocal dispersion of 0.18 Å px^{-1} in the central region of each exposure (roughly, λ4900 Å). For the "red" set-up, we chose an angle of 9°33′, obtaining spectra from λ5700 to λ7900 Å at a reciprocal dispersion of 0.24 Å px^{-1} near λ6600 Å. A Th-Ar lamp was used for wavelength calibration. The usual series of bias and flat-fields were also obtained for each observing night.

The spectra from ESO were obtained with the échelle spectrograph of the 1.52-m telescope (CCD RCA No. 13, 640×1024 pixels) and they were centered around λ4473 Å. The spectral field available extends from 4255 Å to 4630 Å, which contains the Hγ, Fe II 4351, He I 4471 and Mg II 4481 lines. We recorded comparison spectra with a thorium hollow cathode device and we carried out bias and flat-field records by means of a Xenonphot lamp. The entrance slit width was 350 μm, and resolution was $R = 35\,000$ (each spectral element covering 2 pixels) with a binning factor 2 × 1. Dispersion around 4475 Å was 3.54 Å mm^{-1}, the

$S/N \simeq 150$ and the quantum efficiency of the CCD about 67%.

The observations carried at the OHP were obtained using the 1.52-m telescope with the AURELIE spectrometer. The detector has two identical and independent arrays TH7832 with 2048 photodiodes of 13 μm width (Gillet et al. 1994). We used two gratings: No. 2 with 1200 lines mm^{-1} giving a dispersion of 8 Å mm^{-1} and $R = 16\,200$; No. 3 with 600 lines mm^{-1} where the resulting dispersion is 16.5 Å mm^{-1} and $R = 8000$.

2.2. Data reduction

The data reduction was performed by means of software entirely written by one of us (J. Ch.) and the reduction procedure is described in Ballereau et al. (1995).

2.3. The program stars

The program stars are mainly from Slettebak (1982) and Hubert & Hubert (1979). Five stars are from the BS-catalogue (Hoffleit & Jaschek 1982), either because they did not have measured $V \sin i$ or they have been previously studied by Ballerau et al. (1995). The stars observed and the log of observations are given in Table 1. Their MK spectral types are shown in column 4 of this table. They come from several sources: a) the BCD spectrophotometric classification (Moujtahid et al. 1998; Zorec & Briot 1991); b) the classification adopted in Ballereau et al. (1995), which is based mainly on a compilation of spectrophotometric data; c) for those stars for which we do not have data in a) or b), the MK classification is taken from Slettebak (1982). Columns 5 and 6 of Table 1 show the fundamental stellar parameters ($T_{\rm eff}, \log g$) of the program stars, which were used either as reference parameters in the fitting procedure leading to the $V \sin i$, or to estimate several other quantities dealt with in this work. They were derived from the BCD classification system (Divan & Zorec 1982). These fundamental parameters do not correspond to the individual (λ_1, D) values of stars, but to the centroids of the curvilinear quadrilaterals of the BCD classification system which set the respective MK spectral types. In the BCD system, stars are classified according to the value of their Balmer discontinuity (D given in dex) and the mean spectral position of this discontinuity (λ_1 given in Å). D is an effective temperature indicator, while λ_1 is related to the luminosity class (Chalonge & Divan 1973).

2.4. Atlas of line profiles

Figure 1 shows the first page (of 35) of the atlas of normalized profiles of the Hγ line of the 116 Be stars of our program. Figure 2 shows the first page (of 37) of the atlas of normalized profiles of the He I 4471 and Mg II 4481 lines of the program stars. These line profiles have not been smoothed. Our tracings are corrected for Doppler shift due to the Earth movement, but not for the radial velocity of stars. Each panel shows the HD of the star and the date of observation in (NN: year)(NN: month)(NN: day). The Hγ, He I 4471 and Mg II 4481 line profiles are obtainable by individual sets of 6 profiles, each in full page display.

2.5. Measurements performed on the line profiles

Apart from the line profile treatments and measurements relative to $V \sin i$ determination, we carried out a series of preliminary measurements on the lines which accompany the atlas of line profiles.

2.5.1. The Hγ line

Table 2 shows the measurements carried out on the photospheric-like component of the Hγ line: HD number of stars (Col. 1), date of observation in (year)(month)(day) (Col. 2). For all stars, with and without detectable emission, we give the parameters a, b, c and $\lambda_{\rm c}$ which characterize the empirically determined photospheric absorption component of the line profile used to separate the emission component. The meaning of these parameters is explained below in this section and their values are given in Cols. 3–6 of Table 2. For all stars and for each observation date we also measured the central absorption depth of the photospheric-like component, $r_{\rm c} = 1 - (F_{\lambda_{\rm c}}/F^*_{\rm o})$ (Col. 7), where $F_{\lambda_{\rm c}}/F^*_{\rm o}$ is the flux measured at the line center relative to the continuum.

All measurements carried out on the emission component of the Hγ line were performed on profiles corrected for the underlying photospheric-like absorption. In most cases the emission in the Hγ line is small and does not seem to modify considerably the photospheric wings. Nevertheless, the photospheric line is somewhat modified by the veiling produced by the continuum flux excess due to the CE. No sooner does the line emission exceed the local continuum level than the wings of the photospheric-like component change by a significant amount. It then becomes difficult to find a model line profile giving a good fit with reliable fundamental stellar parameters. For this reason, we have decided to separate the emission component by determining the bottom of the photospheric-like absorption using the following empirical line profile:

$$\psi(\lambda) = \exp\{-[a \times (\lambda - \lambda_{\rm c})^b + c]^{-1}\} \quad (1)$$

where a, b and c are constants which are determined using only three points in the observed line profile. Let define $y_i = -[\ln \psi^{\rm obs}(\lambda_i)]^{-1}$ and $x_i = \lambda_i - \lambda_{\rm c}$, where $\lambda_{\rm c}$ is the central wavelength of the observed profile. Two points, x_i ($i = 1,\ 2$) are chosen freely and the third is determined by $x_3 = (x_1 x_2)^{1/2}$. The constants a, b and c are then calculated as follows:

$$\left.\begin{array}{l} c = (y_1 y_2 - y_3^2)/(y_1 + y_2 - 2y_3) \\ \ln(y_i - c) = b \times \ln x_i + a \end{array}\right\}. \quad (2)$$

Line fits with (1) and (2) are supposed to be carried out for stars with rotational velocities $V \sin i \gtrsim 50$ km s^{-1}, for

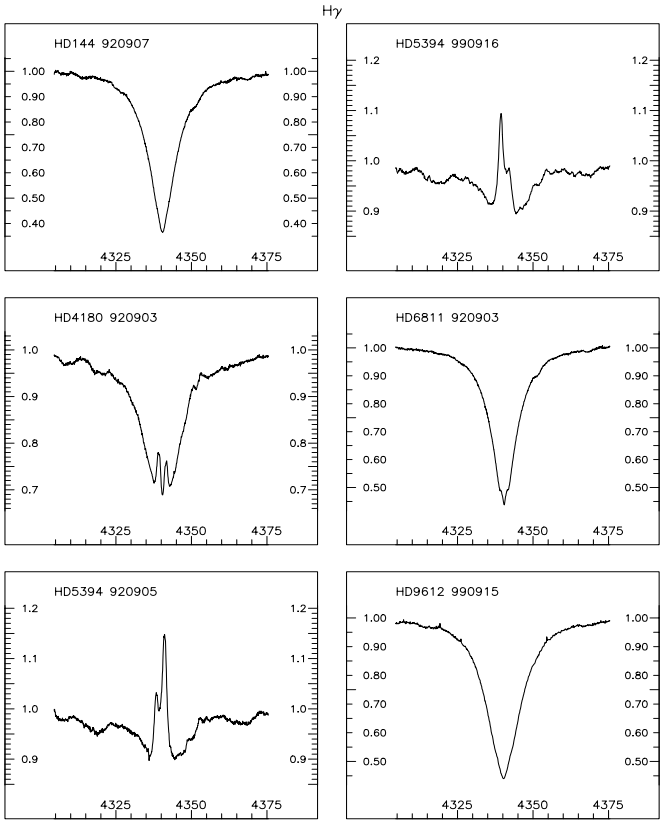

Fig. 1. First page of the atlas of Hγ line profiles.

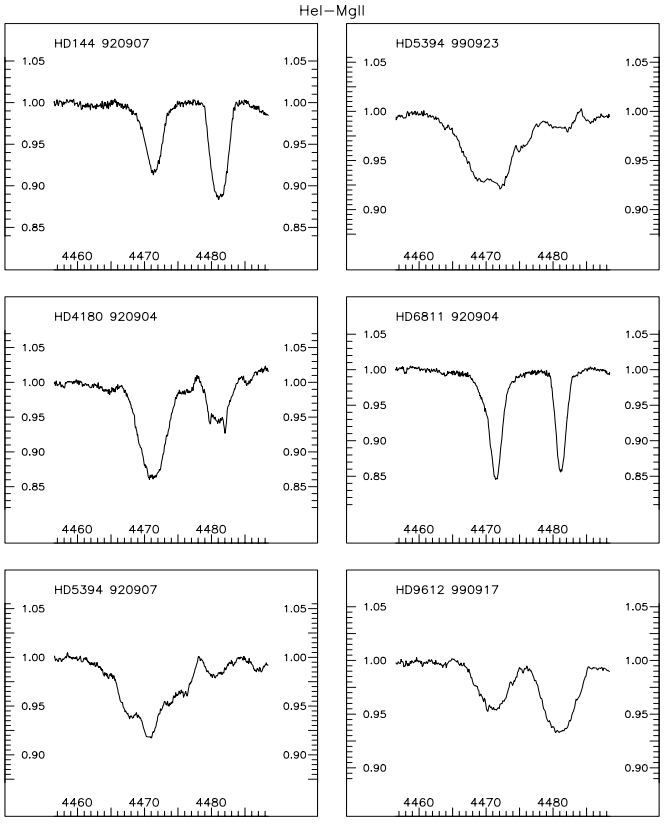

Fig. 2. First page of the atlas of He I 4471 and Mg II 4481 line profiles.

which the non-LTE central absorption dimple in the Hγ line is obliterated. Using model Hγ line profiles to test the quality of the fits, we found that the expected differences between the fit and the observed profiles range as $0.002 \lesssim |(O-C)/C| \lesssim 0.012$ for effective temperatures $10\,000 \leq T_{\rm eff} \leq 50\,000$ K and surface gravities $2.0 \leq \log g \leq 5.0$. Figure 3 shows some typical Hγ line profiles where the photospheric-like component was fitted using relation (1). We note that parameters a, b and c are useful for a quick comparison of line behaviour in other emission/absorption phases of the program Be stars.

Table 2 also gives the measurements made on the emission and shell absorption component in the Hγ line due to the CE. These measurements are: the separation of the emission peaks $\Delta_{\rm p}$ in km s^{-1} (Col. 8); the full width at half maximum $\Delta_{1/2}$ in km s^{-1} (Col. 9); the mean residual peak emission intensity $r_{\rm p} = \overline{(F_{\lambda_{\rm p}} - F^*_{\lambda_{\rm p}})/F^*_{\rm o}}$, where $F^*_{\lambda_{\rm p}}$ is the underlying photospheric-like absorption at the emission peaks wavelengths $\lambda_{\rm p}$ and $F^*_{\rm o}$ is the stellar continuum flux (Col. 10); the intensity at the central absorption in the emission component measured from the photospheric-like profile, $r_{\rm a} = (F_{\lambda_{\rm a}} - F^*_{\lambda_{\rm a}})/F^*_{\rm o}$ (Col. 11); the wavelengths, in $\lambda_{1,2} - 4300$ Å, where the emission rises from the underlying photospheric-like line (Col. 12); in Col. 13 is the equivalent width W_+ in Å, which has two meanings: a) when there is no W_- value in Col. 13, it corresponds to the total emission above the underlying photospheric-like absorption, b) when there is a W_- value, it represents the total emission in both peaks above the underlying photospheric-like absorption profile; Col. 14: the total equivalent width W_- in Å of the absorption below the underlying photospheric-like absorption profile.

Table 2 also gives the measurements corresponding to the Hγ lines of Be stars without detectable CE emission and/or absorption components. In these cases we have: HD number (Col. 1); date of observation (Col. 2); parameters a, b and c of photospheric absorption (Cols. 3–5); $\lambda_{\rm c}$ the wavelength of the centre of the line (Col. 6); the central absorption depth $r_{\rm c}$ (Col. 7).

2.5.2. The He I 4471 line

The measurements corresponding to the He I 4471 line are presented in Table 3. For all measured lines we have: Col. 1 = HD number; Col. 2 = date of the observation presented as (year)(month)(day); Col. 3 = wavelength of the bottom half of the line bisector; Col. 4 = central intensity in the line absorption $F_{\lambda_{\rm c}}/F^*_{\rm o}$; Col. 5 = full width at half maximum $\Delta_{1/2}$ in Å; Col. 6 = wavelengths λ_1 and λ_2, in $\lambda - 4400$ Å; Col. 7 = equivalent width of the line in Å; between which the equivalent width was calculated. For those He I 4471 lines which are heavily blended with the neighbouring Mg II 4481 line, we calculated two equivalent widths. They are given one on top of the other in Col. 7. The first estimate corresponds to the integration between the indicated wavelengths (λ_1, λ_2) and the second is simply twice the equivalent width of the blue half of the

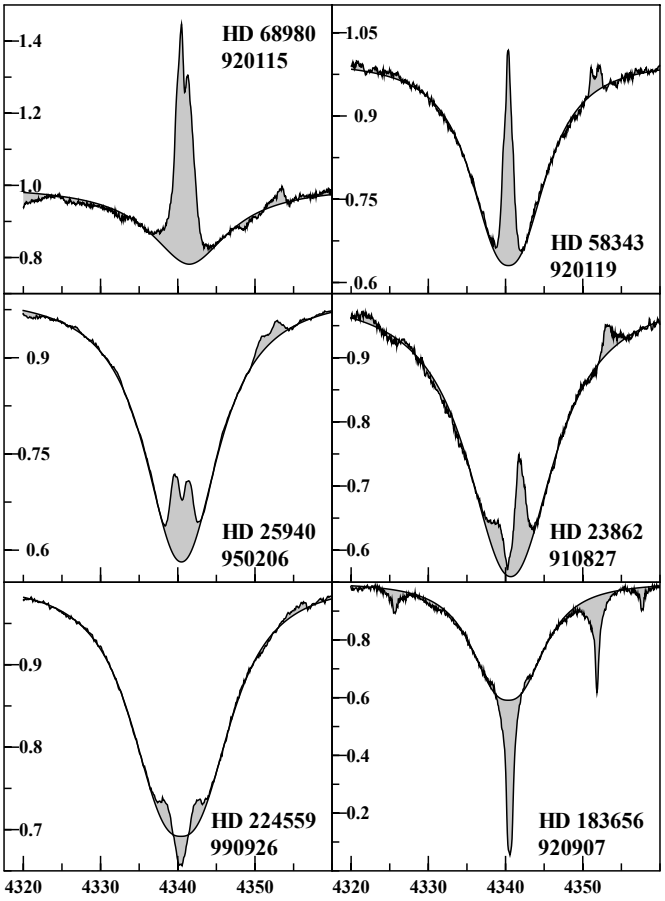

Fig. 3. Examples of empirical fits carried out on the Hγ photospheric-like component in Be stars with CE emission/absorption components of different strengths for "Be" and "Be-shell" phases.

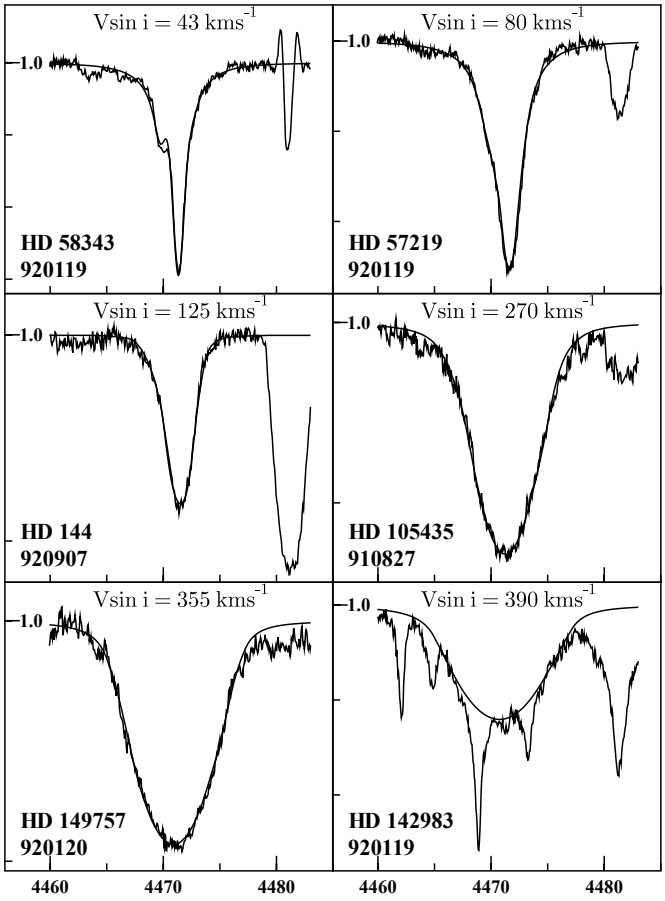

Fig. 4. Examples of typical fits of the observed He I 4471 line in program stars with different $V \sin i$ obtained with non-LTE model line profiles.

line. This last is also preceded by the resulting (λ_1, λ_2) interval.

2.5.3. The Mg II 4481 line

Table 4 gives the measurements carried out on the Mg II 4481 line. This line is sometimes strongly affected by emission, so that the photospheric component cannot be measured. In Table 4 we have: Col. 1 = HD number; Col. 2 = date of observation (year)(month)(day); Col. 3 = wavelength of the minimum in the absorption line; Col. 4 = central intensity in the line absorption; Col. 5 = full width at half intensity; Col. 6 = wavelengths λ_1 and λ_2 (in $\lambda - 4400$ Å) between which the equivalent width in Col. 7 was calculated; Col. 7 = equivalent width (W_1) in Å of the absorption (or absorption component); Col. 8 = total equivalent width (W_2) in Å of the emission components above the continuum. When two emission peaks are seen, we measured the radial velocity of each peak and its intensity. The radial velocities of emission peaks were added in Col. 3 and the intensities were added in Col. 4. The emission peaks are identified by the letters e_1 and e_2 indicated in Col. 2.

2.5.4. The Fe II 4351 line

The Fe II 4351 line is frequently seen in emission on the red wing of the photospheric Hγ absorption component. Each time this line was seen we did the following measurements which are given in Table 5. In Table 5 we have: Col. 1 = HD number; Col. 2 = date of observation (year)(month)(day); Col. 3 = identifiers "e" for an emission peak, "a" for the central absorption and "i" for an inflexion; Col. 4 = wavelengths of the emission peaks and of the central absorption; Col. 5 total intensity, $F_{\lambda_{\rm e,a,i}}/F^*_{\rm o}$, at the emission peaks and/or at the central absorption. Let us note that the net emission intensity in $\lambda_{\rm e,a,i}$ is given by $F_{\lambda_{\rm e,a,i}}/F^*_{\rm o} - \psi(\lambda)$, where $\psi(\lambda)$ is given in (1) and its respective defining constants a, b and c in Table 2.

3. The $V \sin i$ determination

3.1. Fit of observed lines with model line profiles

As compared to B stars without emission, apart from the characteristic line emissions, Be stars show still two significant differences: 1) they have an abnormal continuum energy distribution, which is characterized by variable colour and flux excesses (Moujtahid et al. 1998, 1999); 2) their

mean true linear equatorial velocities are higher than in B stars: $V(\mathrm{Be}) \sim 1.5{-}2.0 \times V(\mathrm{B})$ (Zorec et al. 1990). Due to the mentioned flux excesses (positive or negative), the line profiles can be over (under) normalized as compared to those obtained with normal continuum energy distributions. This effect, also known as the veiling effect, produces spuriously shallowed (deepened) line profiles that may thwart straightforward comparisons with theoretical line profiles. On the other hand, as a consequence of the fast rotation, the spectral types of Be stars as well as their fundamental parameters are aspect-angle dependent quantities, so that they do not reflect their actual masses and evolutionary stages. In order to avoid dealing with model He I 4471 line profiles predicted for uncorrectly chosen fundamental stellar parameters, in the fitting procedure that gives the $V \sin i$, we considered $T_{\rm eff}$ and $\log g$ as free parameters. However, the $T_{\rm eff}$ and $\log g$ produced in this way should not necessarily be considered as representing a new determination of these fundamental parameters. These values, which in fact correspond to uniform stellar atmospheres, only mimic peculiar formation conditions of the observed lines in atmospheres which are deformed by rapid rotation. The theoretical line profiles used to fit the observed He I 4471 line are those calculated by Stoeckley & Mihalas (1973), who used non-LTE models of stellar atmospheres (Mihalas 1972). The reason for this choice is that in these models the line profiles are rotationally broadened by taking into account the full limb darkening of spectral lines. It was shown by Collins & Truax (1995) that convolutions of flux line profiles with rotational broadening functions obtained from monochromatic limb-darkening laws lead to systematic errors in $V \sin i$ estimates. The He I 4471 line profiles calculated by Stoeckley & Mihalas (1973) are however for stars not affected by gravity darkening induced by rapid stellar rotation (von Zeipel 1924).

The line profiles calculated by Stoeckley & Mihalas (1973) are for effective temperatures ranging from $T_{\rm eff} = 15\,000$ K to $27\,500$ K and $\log g = 2.5$ to 4.0 dex. By parabolic interpolation and linear extrapolation from this grid, we have obtained a working grid of 1651 line profiles corresponding to the following intervals of fundamental parameters: $13\,000 \mathrm{\ K} \leq T_{\rm eff} \leq 31\,000$ K at steps $\Delta T_{\rm eff} = 500$ K; $2.5 \leq \log g \leq 4.0$ with steps $\Delta \log g = 0.5$ dex and for 13 values of $V \sin i$ ranging from 0 km s^{-1} to 500 km s^{-1}. In the fitting procedure we have chosen a starting value of the rotational velocity, $(V \sin i)_{\rm o}$, obtained from the He I 4471 line FWHM. As many He I 4471 lines present a number of features due to extra emission/absorption: bumps due to non-radial pulsations; the Mg II 4481 line frequently encroaching on their red wings, we have chosen "clean" regions to achieve the line profile fit. Using the $(V \sin i)_{\rm o}$ we looked for $(T_{\rm eff}, \log g)$ parameters in the working grid of model line profiles that produce the best fits, as controlled by a χ^2 test. The calculation casts 15 best, more or less equivalent fits, regardless of the fundamental parameters adopted. We then selected only those fits whose $[(T_{\rm eff})_{\rm o}, (\log g)_{\rm o}]$ parameters were closest to those chosen for the stellar spectral type. For stars where the fitting procedure suggested that the $[(T_{\rm eff})_{\rm o}, (\log g)_{\rm o}]$ may be outside the intervals of the working grid, we sought the best temperature and gravity by linear extrapolation. We then proceeded to another fitting sequence using a new grid of line profiles interpolated around the parameters $[(T_{\rm eff})_{\rm o}, (\log g)_{\rm o}, (V \sin i)_{\rm o}]$ with steps $\delta T_{\rm eff} = 50$ K, $\delta \log g = 0.05$ dex and $\delta V \sin i = 5$ km s^{-1}.

3.2. Results obtained

3.2.1. $V \sin i$ scale

For each observed He I 4471 line profile we have determined three parameters $(T_{\rm eff}^{\rm fit}, \log g^{\rm fit}, V \sin i)$ that produced the best fit as controlled by a χ^2 test. These parameters were determined for all observation dates of each star. Each observation of a given star was studied as an independent object. As in fast rotators the ratio between the polar and the equatorial local effective temperature can be as high as $T_{\rm p}/T_{\rm e} \simeq 1.23$, in each object we disregarded all $(T_{\rm eff}^{\rm fit}, \log g^{\rm fit}, V \sin i)$ determinations with $|T_{\rm eff}^{\rm fit} - \overline{T_{\rm eff}^{\rm fit}}| > 0.12\overline{T_{\rm eff}^{\rm fit}}$, where $\overline{T_{\rm eff}^{\rm fit}}$ is the average of the individual temperature estimates. The values of $V \sin i$ with the respective 1σ dispersions are given in Table 6 (Col. 2). Column 3 of Table 6 shows the numbers of independent determinations of each $V \sin i$. The adopted averages of parameters $(T_{\rm eff}^{\rm fit}, \log g^{\rm fit})$ produced when determining the $V \sin i$ are presented in Table 6 (Cols. 4 and 5). Figure 4 shows some typical fits of the observed He I 4471 lines with non-LTE model line profiles interpolated from the original Stoeckley & Mihalas' (1973) grid.

In a rapid glance at our $V \sin i$ determinations, in Fig. 5 we compare them with those obtained elsewhere for the same stars. Figure 5a compares our determinations with those of Slettebak (1982). Apart from some particular cases which are discussed below, we see that within a dispersion $\sigma_{V \sin i} \lesssim 30$ km s^{-1}, our $V \sin i_{\rm pw}$ (pw = present work) are in the same scale as Slettebak's (1982) results ($V \sin i_{\rm Sl}$). In Fig. 5a we have also plotted the $V \sin i_{\rm pw} = V \sin i_{\rm Sl}$ relation (full line) and the $\pm\sigma$ lines (dashed lines). Knowing that Slettebak's $V \sin i$ were obtained by taking into account the non-uniform distribution of $T_{\rm eff}$ and $\log g$ induced by the rapid rotation over the stellar surface, we conclude that by keeping free the model $T_{\rm eff}$ and $\log g$, our method of $V \sin i$ determination is, in some way, also sensitive to the rotational effects mentioned. Figure 5b compares Uesugi & Fukuda's (1982) velocities ($V \sin i_{\rm UF}$) with $V \sin i_{\rm Sl}$ of our program stars. It is known that Uesugi & Fukuda's $V \sin i$ were not determined taking into account the rotationally induced changes mentioned above. For the sake of comparison, we have drawn in Fig. 5b the $V \sin i_{\rm UF} = V \sin i_{\rm Sl}$ relation (full line), the $V \sin i_{\rm UF} = V \sin i_{\rm Sl} + 42$ relation (dashed line) and around the latter the corresponding $\pm\sigma$ relations (dotted lines). In Fig. 5b it is apparent that not only there is a higher scatter, $\sigma = 52$ km s^{-1}, but a systematic deviation of 42 km s^{-1}

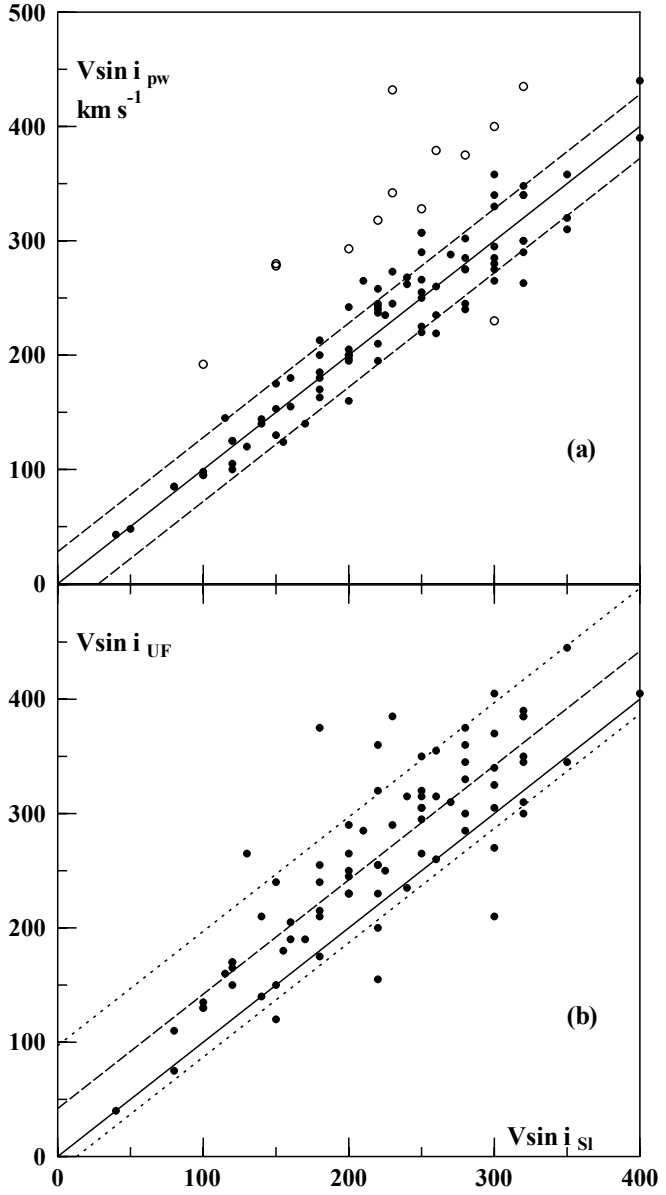

Fig. 5. Comparison of the $V \sin i$ obtained in the present work (pw) with those determined for the same stars by Slettebak (1982, Sl) and given by Uesugi & Fukuda (1982, UF). Figure 5a: open circles ≡ discordant determinations; full line ≡ $V \sin i_{\rm pw} = V \sin i_{\rm Sl}$ relation; dotted lines ≡ $\pm\sigma$ relations. Figure 5b: full line ≡ $V \sin i_{\rm UF} = V \sin i_{\rm Sl}$ relation; dotted line ≡ true $V \sin i_{\rm UF}$ vs. $V \sin i_{\rm Sl}$ relation; pointed lines ≡ $\pm\sigma$ relations.

as well, which was already observed by Slettebak et al. (1975) for normal stars of spectral types B, A and F.

3.2.2. The fitting ($T_{\rm eff}$, $\log g$) parameters

Figure 6a shows the relation between the effective temperature obtained from the line fitting procedure and the effective temperature attributed to the apparent stellar spectral type. Figure 6b shows the $\log g$ obtained from fits as a function of the spectral type dependent $\log g$. Apart from a dispersion $\sigma_{\log T_{\rm eff}} = 0.043$ dex, there is a systematic deviation between both effective temperature estimates. On the other hand, the fitting $\log g$ parameters seem to be independent of the initial surface gravities. This means that the $V \sin i$ determination may be quite sensitive to the model $\log g$ value.

Several effects can be responsible for the differences seen in Fig. 6:

a) The $(T_{\rm eff}, \log g)$ attributed to the studied stars are for average MK spectral type and not for individual (λ_1, D) parameters. According to the spectral type-luminosity class, these differences can be as high as $\Delta T_{\rm eff} \simeq (T_{\rm eff}/370)^2$ K and $\Delta \log g \simeq 4.642 - \log T_{\rm eff}$ dex.

b) The non-homogeneous distribution of $T_{\rm eff}$ and $\log g$ over the stellar surface induced by the fast rotation may lead to a hemisphere averaged spectral type that is interpreted with a set of fundamental stellar parameters which do not necessarily correspond to the local $(T_{\rm eff}, \log g)$ parameters of regions which dominate the formation of the observed lines.

c) As Mihalas' non-LTE model atmospheres were constructed with low line blanketing and a restricted number of continuum absorbers, they have long been known to produce systematic differences in the estimates of fundamental stellar parameters.

d) The He I line profiles are not only sensitive to local line formation conditions and to non-LTE effects, but also to He abundance. Smith et al. (1994) have found that the equivalent widths of some He I lines in pulsating B stars and in Be stars with low emission are stronger than in typical dwarf stars. The CE can contribute with a backwarming effect, which markedly increases the temperature in the outer layers of the stellar atmosphere. The enhancement of He abundance, claimed in recent works (Floquet et al. 2000; Koubský et al. 2000), can be related to mixings due to instabilities triggered by the rapid rotation and to evolutionary effects (Lyubimkov 1996, 1998). These effects together can then favour the appearance of abnormal He I line strengths.

e) Due to the veiling effect, the equivalent width of the observed He I 4471 lines in Be stars is frequently smaller than the value expected for normal B stars with the same spectral type. Mostly in hot Be stars, this effect can lead to systematic overestimation of $T_{\rm eff}$ and to underestimation of $\log g$. These differences will be discussed in full detail elsewhere.

f) Non-radial pulsations produce changing features in the line profiles, which strongly thwart the fit of observed line profiles with the theoretical ones, sometimes leading to unexpected values of $T_{\rm eff}$ and $\log g$.

g) Some emission due to exophotospheric and/or to CE activities may sometimes fill up somewhat the bottom of a line profile. This effect then yields overestimated $V \sin i$ and $T_{\rm eff}$ and underestimated $\log g$.

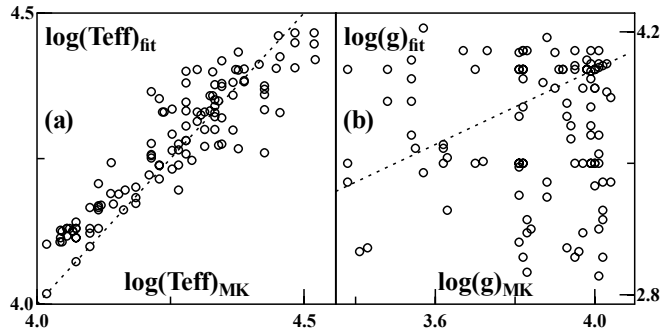

Fig. 6. Comparison between: **a)** parameters $(T_{\rm eff})_{\rm fit}$ obtained in the line fit procedure and $(T_{\rm eff})_{\rm MK}$ associated with the MK spectral types; **b)** parameters $\log(g)_{\rm fit}$ issued from the fits of lines and $\log(g)_{\rm MK}$ for the stellar MK spectral types. The pointed lines represent the $(X)_{\rm fit} = (X)_{\rm MK}$ relations.

3.2.3. Discrepant values of $V \sin i$

Of the 113 $V \sin i$ determined in this work, 13 have values which significantly disagree with those obtained by Slettebak (1982). Some of them are also discordant with those of Uesugi & Fukuda (1982). The discrepant values are shown in Fig. 5a with open circles. Excluding the discordant determinations, the mean quadratic deviation between $V \sin i_{\rm pw}$ and $V \sin i_{\rm Sl}$ is $\sigma = 28$ km s^{-1}. Apart from the 13 most discrepant $V \sin i$ values, there are 4 stars: HD 35439, HD 91120, HD 113120 and HD 208682, with $V \sin i$ which differ by exactly 2σ. The fit of the observed line profiles of these 4 stars with the theoretical profiles does not show any anomaly, except that their spectra are somewhat noisy. In 12 of 13 stars with discrepant values of $V \sin i$, the mean overestimation is $+105 \pm 17$ km s^{-1}. In γ Cas, the 13th discrepant star, our $V \sin i$ is overestimated by $+202$ km s^{-1}! In Fig. 7 we illustrate the difficulties encountered when fitting the observed He I 4471 line profile of these objects. The figure reproduces the fitting parameters $(V \sin i, T_{\rm eff}, \log g)$ corresponding to the solutions shown. For each star we also show the theoretical line profile using Slettebak's (1982) $V \sin i$. The same kind of problems met with in γ Cas (HD 5394) were also found in HD 24534 and in HD 200120 (59 Cyg). Estimations of $V \sin i$ for γ Cas approaching 400 km s^{-1} have been also reported by Yang et al. (1988) and Harmanec (2000). The type of distortions found on the red line profile wing of γ Cas appears in 59 Cyg in the blue wing. The fit shown for HD 56014, which looks quite normal, has entirely the same aspect in HD 20226, HD 28497, HD 33328, HD 63462, HD 110432 and HD 212571. We note that other choices of $T_{\rm eff}$ and $\log g$ would not help to obtain lower values of $V \sin i$ for these stars. Other fitting attempts, such as those shown in Fig. 7 for HD 58978, lead to nearly the same value of $V \sin i$. The narrow absorption in the centre of the line corresponds to $V \sin i = 22$ km s^{-1}. The central absorption in the He I line of HD 131492 we actually fitted, is superimposed on a wide, irregular and variable dimple, which produces by itself even higher value of $V \sin i$ than

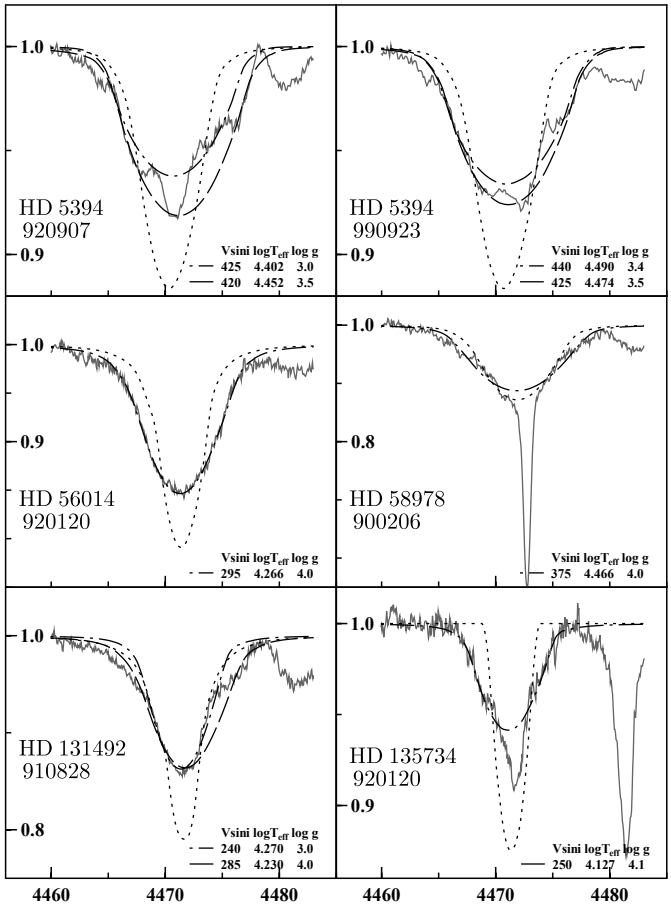

Fig. 7. Typical examples of the He I 4471 line profile fit attempts in stars with discrepant values of $V \sin i$. The corresponding stellar parameters are given for the different attempts. The dotted lines represent the line profiles calculated for the $V \sin i$ given by Slettebak (1982).

those shown in the figure and which tend to smooth out the nearby Mg II line. The line profile of this star observed on 900 206 is similar to the one shown in Fig. 7. Its best fit produces $T_{\rm eff} = 21\,700$ K and $\log g = 3.0$ and $V \sin i = 180$ km s^{-1}. The He I 4471 line profile of HD 135734 seems to have two components. The narrow component leads to a similar $V \sin i$ as for the Mg II 4481 line: $V \sin i = 67$ km s^{-1}, which does not compare either with 150 km s^{-1} given by Slettebak (1982) or with the 400 km s^{-1} given by Uesugi & Fukuda (1982).

The discrepancies in the $V \sin i$ values of these objects are three times larger than the deviations expected from the non-uniformities in $T_{\rm eff}$ and $\log g$ induced in the stellar surface by effects related to the rapid rotation. Unless the line profiles studied by Slettebak (1982) of these stars presented some particular difficulties, such as temporary shell-like absorptions, the differences can still be explained assuming that these objects are binaries. The high $V \sin i$ would then reflect the sum of two independent rotationally broadened line profiles. The possible binarity of 59 Cyg was suggested by Tarasov & Tuominen (1987) and confirmed by Rivinius & Štefl (2000).

4. Correlations between empirical quantities

4.1. Line widths as functions of $V \sin i$

Since the pioneering correlations found by Struve (1931) between the full width at half maximum, $\Delta_{1/2}$, of Balmer emission lines and the $V \sin i$ in Be stars, which raise the hypothesis of rotationally supported CE, a huge amount of later work with similar arguments drawn from studies of hydrogen emission lines as well as from metals, has come to the same conclusions (references in Slettebak & Reynolds 1978; Andrillat & Fehrenbach 1982; Andrillat 1983; Hanuschik 1989; Andrillat et al. 1990; Dachs et al. 1986, 1992; Slettebak et al. 1992; Ballereau et al. 1995). Inasmuch as these papers concern Balmer lines, they mainly refer to Hα and Hβ lines, where emission is stronger. However, fewer works pay attention to the Hγ line or to higher Balmer terms, where emission is fainter and for which spectra with good resolution and high S/N ratios are required. As the regions in the CE where Hγ emission originates are, on average, closer to the central star than those concerned by Hα and Hβ emission lines, the study of the emission of this line may help us to gather information about the physical characteristics of CE layers close to the central star. In this paper we show some correlations concerning only the separation of the double peaks, $\Delta_{\rm p}$, the full width at half maximum, $\Delta_{1/2}$, and the equivalent width, W, with $V \sin i$. We avoided the use of the full width at the base ($\Delta_{1.0}$), since it is strongly dependent on electron scattering broadening and on the quality of photospheric absorption component determination.

The main information we can draw from correlations involving the measured quantities in the Hγ line emission component is resumed in Fig. 8. Figures 8a and 8b show respectively the correlations between $\Delta_{\rm p}$ and $\Delta_{1/2}$ with $V \sin i$. In spite of the high scatter around a mean trend, smaller however than that currently observed for Hα and Hβ lines, this type of result is currently interpreted as revealing rotationally supported CE and hence, that the CE must be flattened with increased density towards the equatorial plane. On theoretical grounds such flattened CE are supported by models based on a number of basic ad hoc assumptions: rotationally driven mass fluxes (Limber 1964, 1967), Keplerian motion of isothermal and inviscid circumstellar gas (Hummel 1994), rotationally wind-compressed discs (Bjorkmann & Cassinelli 1993), bi-stability of radiation driven winds (Lamers & Cassinelli 1999), axisymmetric radiative wind model with ad hoc latitudinal viscosity laws (Stee & Araujo 1994). Solutions based on kinetic theory of inviscid gaseous envelopes, where the azimuthal velocity distribution in the CE satisfies conditions of uniformity near the central star and conservation of angular momentum at increasing distances from the star, lead to CE envelope structures which are far from being flat (Rohrmann 1997). These velocity laws agree with the behaviours deduced for Be stars: $v_\phi \propto (r \sin\theta)^{-j}$ (r distance from the center of the star; θ colatitudinal angle) with $j = 0.8$ (Hanuschik et al. 1988); $j = 1.0$ (Hanuschik 1988); $j = 1.4$ (Mennickent et al. 1994) and other intermediate values between 0.5 and 1.0 (Hummel & Vrancken 2000). They have already been interpreted, however, as corresponding to flattened CE.

Figures 8a and 8b show the respective relations between the line widths $\Delta_{\rm p}$, $\Delta_{1/2}$ and the $V \sin i$. The linear relations shown:

$$\left.\begin{array}{ll} \overline{\Delta_{\rm p}} = 0.75 \times V \sin i + 25 & {\rm kms}^{-1} \\ \overline{\Delta_{1/2}} = 0.83 \times V \sin i + 137 & {\rm kms}^{-1} \end{array}\right\} \quad (3)$$

are not least squares fits. They were sought in order to produce the smallest possible scatter of points in further correlations involving the normalized line widths $\Delta_{\rm p,1/2}/\overline{\Delta_{\rm p,1/2}}$.

Figure 8c shows $\ln \Delta_{\rm p}/\overline{\Delta_{\rm p}}$ against $\ln W_{\rm H\gamma}^{\rm em}$ ($W_{\rm H\gamma}^{\rm em}$ is the equivalent width of the Hγ line emission component). A similar relation, not shown here, is obtained for $\Delta_{1/2}/\overline{\Delta_{1/2}}$. We note that the $\ln \Delta_{\rm p}/\overline{\Delta_{\rm p}}$ against $\ln W_{\rm H\gamma}^{\rm em}$ relation has a slope which cannot be reduced to zero by using other $\overline{\Delta_{\rm p}} = a_{\rm o} V \sin i + a_1$ expressions to normalize $\Delta_{\rm p}$. This slope is expected, however, to be null if $\Delta_{\rm p}$ had to be determined by effects related only to $V \sin i$.

Figure 8d shows the relation between $\ln W_{\rm H\gamma}^{\rm em}$ and $\ln(2V \sin i/\Delta_{\rm p})$, which according to Huang's (1972) assumptions should represent the variation of the emission intensity with the size of an optically thin emitting CE. In Fig. 8d there are two extreme linear relations:

$$\left.\begin{array}{l} \ln W_{\rm H\gamma}^{\rm em} = 3.11 \times \ln(2V \sin i/\Delta_{\rm p}) - 5.03 \\ \ln W_{\rm H\gamma}^{\rm em} = 1.95 \times \ln(2V \sin i/\Delta_{\rm p}) - 1.66 \end{array}\right\}. \quad (4)$$

If the CE regions which are responsible for the Hγ emission were optically thin, we would expect to have $W_{\rm H\gamma}^{\rm em} \propto (R_{\rm e}/R_*)^2 = (2V \sin i/\Delta_{\rm p})^{2/j}$. Relations (4) would then imply:

$$\left.\begin{array}{l} 1.95 \leq 2/j \leq 3.11 \\ 0.64 \leq \ \ j \ \ \leq 1.02 \end{array}\right\} \quad (5)$$

which are nearly the same as that obtained by the authors cited above. From the results obtained in Sect. 5.6 it will be clear that it is worthless to interpret the relation between $W_{\rm H\gamma}^{\rm em}$ and $2V \sin i/\Delta_{\rm p}$ in terms of a given value of j, unless the optical depth in the line be very low.

In the following sections we study the dependence of the observed quantities related to the Hγ line emission component with model-derived parameters, such as the aspect angle under which is seen the system star+CE and the opacity of CE in the Hγ line transition.

4.2. Line emission strength as a function of $T_{\rm eff}$

Figure 9a shows there is a close relation between the average intensity in the Hγ line emission peaks $r_{\rm p}$ and the equivalent width $W_{\rm H\gamma}^{\rm em}$ of its emission. Hence, we do not study the equivalent width separately, as the correlations involving $W_{\rm H\gamma}^{\rm em}$ have the same characteristics as those concerning $r_{\rm p}$. Figure 9b shows $r_{\rm p}$ as a function of $T_{\rm eff}$. We see that as a function of the effective temperature, there

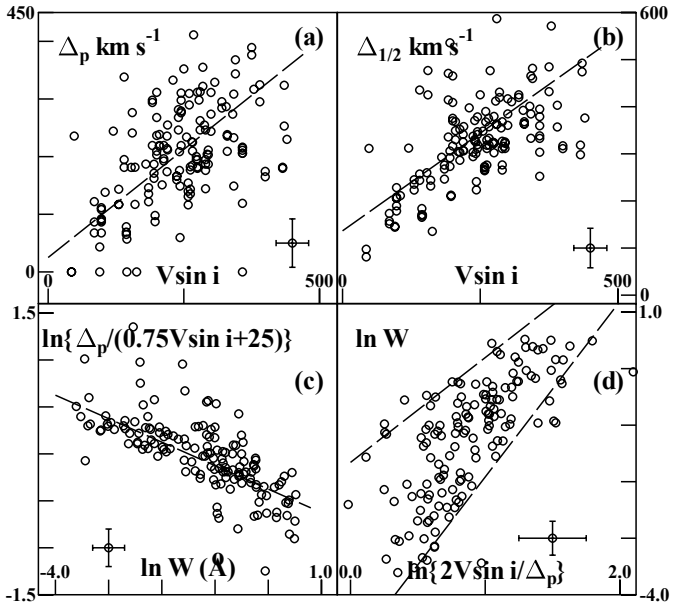

Fig. 8. Correlations involving the Hγ line emission component; **a)** separation of the emission peaks $\Delta_{\rm p}$ against $V \sin i$; **b)** full width $\Delta_{1/2}$ against $V \sin i$; **c)** ln of $\Delta_{\rm p}$ normalized to $0.75V \sin i + 25$ against ln of the equivalent width $W = W_{\rm H\gamma}^{\rm em}$; **d)** $\ln W_{\rm H\gamma}^{\rm em}$ against the ln of $2V \sin i/\Delta_{\rm p}$.

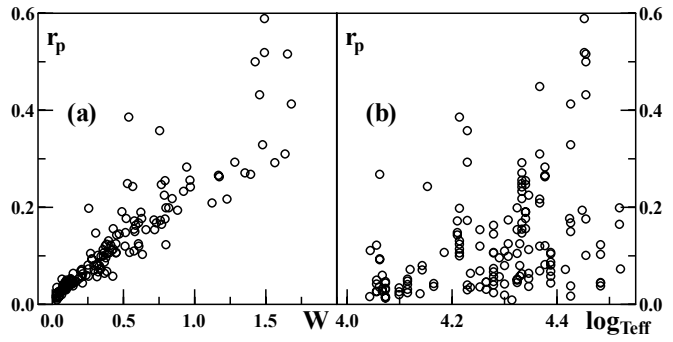

Fig. 9. a) Correlation between the mean residual intensity in the peaks $r_{\rm p}$ of the Hγ line emission component and its equivalent width $W_{\rm H\gamma}^{\rm em}$ in Å. **b)** Relation between $r_{\rm p}$ and the effective temperature.

is an upper limit to the average emission intensity in the peaks given roughly by $r_{\rm p} \simeq -4.4 + 1.1 \times \log\ T_{\rm eff}$. The equivalent relation for the equivalent width is $W_{\rm H\gamma}^{\rm em} \simeq -16.96 + 4.24 \times \log T_{\rm eff}$.

5. Correlations between observed parameters and model derived quantities

In a CE with uniform temperature $T_{\rm e} = 0.8 \times T_{\rm eff}$ and density distribution $\rho \propto R^{-\alpha}$ ($\alpha \sim$ 2–3), it is expected that the extents of the Hα, Hβ and Hγ formation regions, defined as those contributing up to 99% to the total line emission, are roughly $R_{\rm f}({\rm H}\alpha) \simeq R_{\rm f}({\rm H}\beta) \simeq 1.5$ to $9R_*$ and $R_{\rm f}({\rm H}\gamma) \simeq 1.2$ to $2.6R_*$ for a variety of mass-loss rates (Rohrmann 2000). This means that study of the emission and/or shell absorption in the Hγ line can provide

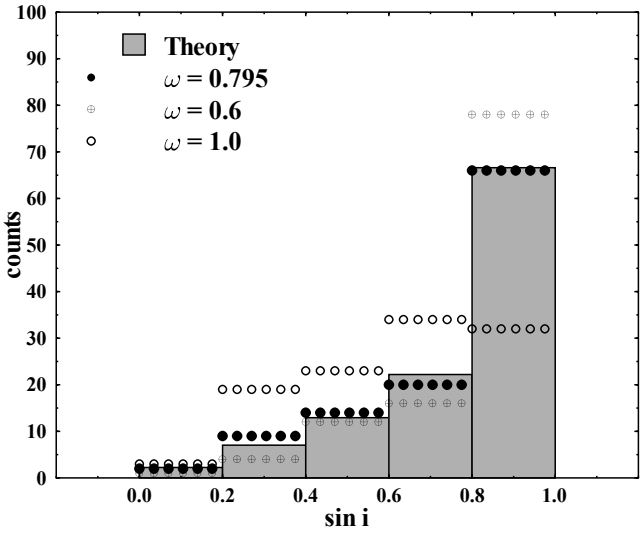

Fig. 10. Distribution of $\sin i$ of the observed stars for different values of the ratio of angular velocities $\omega = \Omega/\Omega_{\rm c}$.

valuable information on the physical and geometric characteristics of the CE layers which are quite close to the central star. The study of these regions is important, because their properties are related to the photospheric and exo-photospheric activities and to the type of mass ejection, continuum or discrete, which are responsible for the formation of the CE.

The aim of this section is thus to obtain statistical information on the behaviour of the Hγ line emission component as a function of some leading physical parameters related to its formation in the CE.

5.1. Aspect angle estimation

All parameters concerning the region of the Hγ line emission formation derived in the present work are studied as a function of the inclination angle i of the stellar rotation axis. To obtain an estimate of i we assume that all stars are rigid rotators. From models of rigidly rotating stars (Sackmann & Anand 1970; Bodenheimer 1971; Clement 1979; Zorec et al. 1988) we draw the following relations:

$$\left.\begin{array}{l} V(\omega) = V_{\rm c} \left(\frac{\Omega}{\Omega_{\rm c}}\right) \left[\frac{R_{\rm e}(\omega)}{R_{\rm c}}\right] \\ \frac{R_{\rm e}(\eta)}{R_{\rm c}} \simeq 0.725 + 0.276 \times \eta \\ \eta = \left[\frac{\Omega}{\Omega_{\rm c}}\right]^2 \left[\frac{R_{\rm e}(\eta)}{R_{\rm c}}\right]^3 \end{array}\right\} \quad (6)$$

where $V_{\rm c}$ is the equatorial critical velocity, $R_{\rm e}(\omega)$ and $R_{\rm c}$ are respectively the equatorial radii at $\omega = \Omega/\Omega_{\rm c}$ and $\omega = 1.0$ (Ω is the angular velocity). For $R_{\rm c}/R_{\rm o}$ and $R_{\rm e}(\omega)/R_{\rm c}$ ($R_{\rm o} = R_{\rm e}(\omega = 0)$) we have neglected small mass dependency on the stellar mass.

From the fundamental stellar parameters, chosen according to the spectral type and masses read in Schaller's et al. (1992) evolutionary tracks, we can easily estimate their equatorial critical velocity $V_{\rm c}$. The ratios between $V \sin i$ and $V_{\rm c}$ are then cleaned up from differences in stellar masses and evolutionary stages, so that their averages

are meaningful for the studied stellar set taken as a whole. We obtain:

$$\overline{V \sin i/V_{\rm c}} = 0.65; \qquad \overline{V/V_{\rm c}} = 0.83 \tag{7}$$

and the respective dispersions:

$$\sigma_{(V \sin i/V_{\rm c})} = 0.24; \qquad \sigma_{(V/V_{\rm c})} = 0.03. \tag{8}$$

For (7) and (8) we used the known relations of Chandrasekhar & Münch (1950) between the projected and the true rotational velocities. The extremely low value of the dispersion of ratios of true equatorial velocities implies that *all studied Be stars rotate at nearly the same ratio* $V/V_{\rm c} \simeq 0.83$, which translated into a ratio of angular velocities represents $\overline{\omega} \simeq 0.87$. This value is very close to $\overline{\omega} = 0.90$ assumed by Slettebak et al. (1992). If all Be stars rotated at the same $\overline{\omega}$, we could then obtain another estimate of $\overline{\omega}$ by seeking the angular velocity ratio that better reproduces the distribution of $V \sin i/V_{\rm c}$ for randomly oriented rotational axes. The theoretical distribution of the ratio $V \sin i/V_{\rm c}$, where $V(\omega)/V_{\rm c} =$ constant can easily be calculated, is shown in Fig. 10. Using the measured $V \sin i$ and relations (6) we sought the $\overline{\omega}$ which closely fits the theoretical distribution shown in Fig. 10 (shaded histogram). We thus obtained $\overline{\omega} = 0.795$. This value which agrees with that found by Moujtahid et al. (1999), where the authors have shown that main sequence Be stars have an ω distribution that strongly peaks at $\omega = 0.8$ and that about 80% of them have angular velocities in the range $0.6 \lesssim \omega \lesssim 1.0$. For the sake of comparison, we then show in Fig. 10 the distributions of $\sin i$ obtained for $\overline{\omega} = 0.6$ and $\overline{\omega} = 1.0$. As the fit for $\overline{\omega} = 0.90$ is far from being the best, we adopted $\overline{\omega} = 0.795$ to derive the inclination angle i of our program stars. The values of $V_{\rm c}$ are given in Table 6, Col. 6, and those of i for $\overline{\omega} = 0.795 \pm 0.2$ are given in Col. 7.

The value of the mean ratio $\overline{V \sin i/V_{\rm c}}$ of Be stars was dicussed in three recent papers (Porter 1996; Steele 1999; Yudin 2001). Using Slettebak's (1982) sample, Porter (1996) obtained $\overline{V \sin i/V_{\rm c}} \simeq 0.52$. From a set of 58 Be stars, Steele (1999) obtained a global $\overline{V \sin i/V_{\rm c}} \simeq 0.41$, though this average shows some luminosity class dependence. Yudin (2001) derived values of $\overline{V \sin i/V_{\rm c}}$ which, according to the spectral type-luminosty class groups, range from 0.38 to 0.65. Porter's $V \sin i$ and ours are referenced to the same scale and lead to nearly the same global mean values for the common stars: $\overline{(V \sin i)_{\rm Po}} = 223 \pm 76$ km s^{-1}, $\overline{(V \sin i)_{\rm pw}} = 236 \pm 86$ km s^{-1}. However, the spectral classifications differ on average about 1 sub-class in spectral type and/or luminosity class, sources of stellar masses and radii are not the same and our $V_{\rm c}$ estimates are luminosity class dependent. For the common stars, all these differences lead to the mean ratio of critical velocities $\overline{(V \sin i)_{\rm pw}/(V \sin i)_{\rm Po}} = 0.78 \pm 0.10$, which accounts entirely for the difference between Porter's and our results. Steele (1999) follows Porter's (1996) way of calculating $V_{\rm c}$ and uses a sample of Be stars where not only $\overline{(V \sin i)_{\rm St}} = 177 \pm 61$ km s^{-1}, but also there is no star with $V \sin i/V_{\rm c} \gtrsim 0.7$. This may mean that in his sample there is some selection effect which favors the lower $V \sin i$ values. From Porter's and Steele's samples we have $\overline{(V \sin i)_{\rm St}}/\overline{(V \sin i)_{\rm Po}} = 0.78$, which explains the low $\overline{V \sin i/V_{\rm c}}$ derived by Steele. Yudin's (2001) data compilation also lead to a global average $\overline{V \sin i/V_{\rm c}} \simeq 0.52$. The luminosity class effect in the $\overline{V \sin i/V_{\rm c}}$ ratio he founds is in the opposite sense than the one found by Steele (1999). However, while Steele's (1999) sample is not large enough to warant a random distribution of i in each luminosity class sub-group, the spectral classification of quite a few stars in Yudin's sample need to be revised.

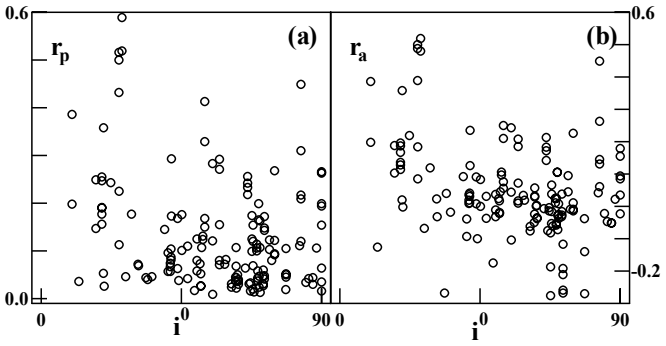

Fig. 11. Mean residual intensity in the emission peaks $r_{\rm p}$ **a)** and in the absorption-like reversal $r_{\rm a}$ **b)** against the aspect angle i.

5.2. Hγ emission intensity as a function of the angle i

In this paper we only deal with the average residual intensity in both emission peaks, $r_{\rm p}$, and the central residual flux in the absorption superimposed to the emission in the Hγ line, $r_{\rm a}$. Figures 11a and 11b show $r_{\rm p}$ and $r_{\rm a}$ as functions of the aspect angle i.

In a disc-shaped CE the optical depth is proportional to $\sec i$ and the residual intensity $r_{\rm p}$ in a line is dependent on the source function factor $S_{\rm l} R_{\rm e}^2 \cos i$ ($S_{\rm l}$ = source function $R_{\rm e}$ = equatorial radius of the CE; see Sect. 5.4.2). Knowing that radiation transfer effects respond exponentially to the optical depth changes with i, we expect that genuine disc-shaped CE will produce a flat distribution of $r_{\rm p}$ and $r_{\rm a}$ against the aspect angle i, followed by a strong drop of emission intensity at inclinations approaching $i = \pi/2$. Except for a few values of $r_{\rm p}$ near $i \simeq 20^{\rm o}$ and $r_{\rm a}$ near $i \simeq 20^{\rm o}$ and $i \simeq 70^{\rm o}$ which deviate in Fig. 11 from rough horizontal strips of values, there is no clear indication for disc-shped CE. In a stellar set, where inclinations i are distributed at random, the following ratio of numbers of stars $N(i < 45^{\rm o})/N(i > 45^{\rm o}) = 0.414$ is expected. In our sample we have $N(i < 45^{\rm o})/N(i > 45^{\rm o}) = 0.398$, which may prevent aspect-angle dependent systematic effects in statistics. To proceed with a numerical description of results shown in Fig. 11, we rebinned the data in two different ways: by $\Delta i = 18^{\rm o}$ steps and by $\Delta \cos i = 0.2$ intervals, so as to have about the same number of points in each bin. All tendencies and/or correlations are,

however, better defined with the $\Delta \cos i$ = constant option. The mean values of $r_{\rm p}$ and $r_{\rm a}$ per $\Delta \cos i$-bin and the respective 1σ dispersions are:

$\Delta \cos i$	=	1.0–0.8	0.8–0.6	0.6–0.4	0.4–0.2	0.2-0.0
$\overline{r_{\rm p}}$	=	0.217	0.116	0.108	0.091	0.131
$\sigma_{\rm p}$	=	0.164	0.086	0.092	0.059	0.100
$\overline{r_{\rm a}}$	=	0.163	0.036	0.010	−0.034	−0.064
$\sigma_{\rm a}$	=	0.193	0.087	0.168	0.103	0.291

Thus, we see that $\overline{r_{\rm p}}$ distributes around a mean value $\overline{r_{\rm p}} = 0.112 \pm 0.102$, except for the first bin, where according to the Student's test, points can be in the same uniform distribution only within a level of significance of 75%. However, a linear decrease with $\cos i$ (correlation coefficient $R = -0.95$) is observed for $\overline{r_{\rm a}}$. Neither for $\overline{r_{\rm p}}$ nor for $\overline{r_{\rm a}}$ does exist a sudden drop of values at $i \simeq \pi/2$. This means that, though *some flattening should not be discarded, data do not show clear indications for strongly flattened CE regions concerned by the Hγ line emission.* The expected mean flattenings (ellipticities) of these CE regions are estimated in Sect. 5.5.1.

5.3. Puzzling line profiles

In our stellar sample there are 89 stars for which we could obtain residual emission line profiles $(F_\lambda - F^*_\lambda)/F^*_{\rm o})$. Assuming that the rotation axis of these objects are oriented at random, we expect that among them only 17 stars are seen at $i \lesssim 36^{\rm o}$. Notwithstanding this small inclination, 35% of them show shell-like Hγ line profiles. On the other hand, there are cases like HD 58343, where the Hγ line emission profile could also be compatible, among other geometrical configurations, with a flat CE seen at $i \sim 10^{\rm o}$. At the same time, the flat disc cannot account, however, for the double peak-behaved Fe II 4351 line emission profile (see Fig. 3). This type of behaviour can also be found in many cases displayed in Hanuschik's et al. (1996) atlas of Be Balmer and Fe II line profiles.

Hence, we cannot assume that for all Be stars the CE near the central star is simply a flat disc.

5.4. The Hγ line optical depth

5.4.1. The model

Because the formation region of the Hγ line emission and/or "shell" component in the CE is not very extended, to obtain a first insight on the mean value of physical parameters which characterize this region, we reduce it to an equivalent emitting/absorbing geometrically thin shell (the word "shell" has here its literary meaning and not the known spectroscopic one used for Be stars). The global geometry of this shell must however be formulated in order to be able to account qualitatively for different structures, from ellipsoidal to flattened disc-shaped CE. Flat discs are currently suggested to interpret observations of Be stars. There are however strong arguments against the use of such a representation for every circumstance (Moujtahid et al. 1998, 1999). According also to conclusions in Sects. 5.2 and 5.3, we opted for an ellipsoidal equivalent shell. The occurrence of a possible flattened disc can be represented leaving the ellipticity parameter $E \rightarrow 0$. In spite of the many simplifying assumptions required in this representation, it is still about the only method which can be applied to a high number of objects in order to obtain statistical trends which are not influenced by a priori geometrical and physical structures that are necessarily imposed to models in detailed radiative transfer calculations. Thus, Moujtahid et al. (1999) have shown that the radiation flux produced by the system star+equivalent ellipsoidal shell can be represented with a relation of the type:

$$F_\lambda = F^*_\lambda {\rm e}^{-\tau_\lambda} + \mathcal{E}(S_{\rm l}, R_{\rm e}, E, i, \tau_\lambda) \quad (9)$$

where the first term on the right stands for the absorption produced by the effective circumstellar layer of photospheric radiation at the wavelength λ; $F^*_\lambda = F^*_{\rm o}\Phi^*(\lambda)$ is the flux emitted by the central star ($F^*_{\rm o}$ is the local photospheric continuum flux; $\Phi^*(\lambda)$ is the photospheric line profile); $\mathcal{E}$ describes the total emission produced by the equivalent shell and whose final form depends on the one hand, on the apparent geometrical configuration of the CE and on the other hand, on the line wavelength analyzed. In this term: $S_{\rm l}$ is the line source function; $R_{\rm e}$ is the radius of the equivalent shell; E is the ellipticity of the shell; i is the aspect angle under which the star+CE system is seen; τ_λ is the (E, i)-dependent optical depth of the shell at the line wavelengths.

As we are interested only in general trends of the observed parameters as a function of the CE derived parameters, for the sake of simplicity we assume that the ellipsoidal CE covers the central star, whatever the angle i under which the star+CE system is seen. The minimum height of a possible disc-shaped CE is then reduced to the stellar radius, $H_z \simeq R_*$.

Correlations of $\Delta_{\rm p}$ and $\Delta_{1/2}$ with $V \sin i$ imply that the velocity field in the studied CE region has a strong azimuthal component. So, the loci of constant radial velocities, $v_{\rm r}$, form a dipole-field pattern, where only the curves corresponding to the lower radial velocities are seen by the observer as projected towards the disc of the underlying star (Horn & Marsh 1986). This allows us to separate the representation of fluxes in wavelengths near the core of the emission line from fluxes in the emission peaks and in the wings. Thus, the flux emitted by the CE in the central absorption-like reversal in the Hγ emission component is described by:

$$\mathcal{E}(v_{\rm r} \sim 0) = \pi R^2_* S_{\rm l}(1 - {\rm e}^{-\tau_\lambda}) + 2[R_{\rm e}\Lambda^{1/2}(E, i) - R_*]R_* S_{\rm l}(1 - {\rm e}^{-2\tau_\lambda}) \quad (10)$$

where the first term on the right stands for the emission of the CE surface facing the central star and the second

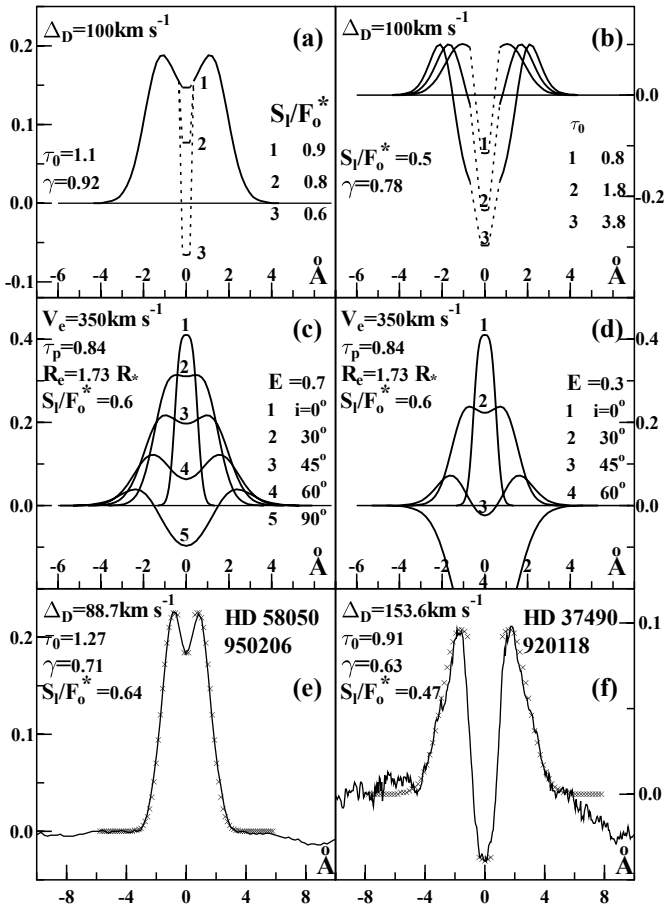

Fig. 12. Model Hγ line emission profiles: **a)** line profiles for given γ and $\tau_{\rm o}$ and several values of $S_{\rm l}/F^*_{\rm o}$; **b)** line profiles for given γ and $S_{\rm l}/F^*_{\rm o}$ and several values of $\tau_{\rm o}$; **c)** line profiles given by relation (9) and (11) for a CE with ellipticity $E = 0.7$ and the noted parameters and for several inclination angles i; **d)** same as **a)** but for ellipticity $E = 0.3$; **e)** and **f)** are fit examples of observed Hγ line emission residual profiles $(F_\lambda - F^*_\lambda)/F^*_{\rm o}$.

term represents the emission coming from the upper and lower rectangular-like strips of the CE with radial velocities $v_{\rm r} \sim 0$.

The emission flux in the peaks and the wings is given by:

$$\mathcal{E}(\text{wings}) = \pi[R_{\rm e}^2 \Lambda(E,i) - R_*^2] S_{\rm l}(1 - {\rm e}^{-2\tau_\lambda}). \quad (11)$$

In (10) and (11) the factor $\Lambda(E,i)$ accounts for the ellipticity of the CE equivalent shell and its effective emitting surface as seen according to i:

$$\Lambda(E,i) = [1 - (1-E^2)\sin^2 i]^{1/2}. \quad (12)$$

We readily see that for $E \to 0$ we obtain $\Lambda(E,i) = \cos i$ suitable for discs.

We note that $R_{\rm e}/R_*$ does not represent the actual total extent of the studied line emission formation region. Roughly, it represents the distance at which the gas density, if distributed as $\rho(R) = \rho_{\rm o}(R_*/R)^\alpha$, will attain its self-averaged value $\overline{\rho} = \rho_{\rm o}[(\alpha-1)/(2\alpha-1)]$. Thus, $R_{\rm e}/R_* = [(\alpha-1)/(2\alpha-1)]^{-1/\alpha}$ (Moujtahid 1998).

The optical depth is also sensitive to the flatness of the CE through the factor $\Lambda(E,i)$ (Moujtahid et al. 1999):

$$\tau_\lambda = \tau^p_\lambda / \Lambda(E,i) \quad (13)$$

where τ^p_λ is the optical depth of the equivalent shell measured in the polar direction z. It is given by:

$$\tau^p_\lambda = \frac{\pi e^2}{mc} f \int N(z) \Phi(\lambda, \Delta\lambda_{\rm th}, z) {\rm d}z \quad (14)$$

where $N(z)$ is the number density distribution of absorbers in the z-direction and $\Phi(\lambda, \Delta\lambda_{\rm th}, z)$ is the local absorption profile ($\Delta\lambda_{\rm th}$ is the thermal Doppler shift). In this work we assumed that the result of the integration in (14) might be represented as:

$$\int N(z)\Phi(\lambda, \Delta\lambda_{\rm th}, z){\rm d}z \propto N_{\rm T} \frac{1}{\sqrt{\pi}\Delta_{\rm D}} {\rm e}^{-(\frac{\lambda-\lambda_{\rm o}}{\Delta\lambda_{\rm D}})^2} \quad (15)$$

where $N_{\rm T}$ is the column density of absorbers in the z-direction and $\Delta_{\rm D}$ is an effective velocity which accounts in a statistic way for the whole velocity field in the formation region of the line (Höflich 1988). $\Delta_{\rm D}$ acts as a free line profile fitting parameter. It masks, however, the little-known physics of line formation in the moving CE of Be stars. We will not conjecture any further interpretation of $\Delta_{\rm D}$.

It is possible that among the approximations made in the above representations, the one given by (15) is perhaps the most open to criticism. This approximation can, however, mimic fairly closely the resulting non-trivial analytical expressions for line profiles Doppler-broadened by velocity fields of "first kind" (Huang & Struve 1953). The expression is exact for profiles resulting in a CE where $N(z)$ and $\Phi(z)$ are both Gaussian (Horn & Marsh 1986; Hanuschik 1995). This relation also holds for a region where there is a randomly distributed velocity field or a large-scale turbulence, for which we could assume that the density distribution of absorbers is $N(z) \sim$ constant. This last approximation could then be appropriate for regions in the CE with colliding clouds of matter produced by recurrent episodes of discrete mass ejections and subsequently eroded by the continuous stellar winds near the central star (Zorec 1981; Zorec et al. 2000). Approximation (15) was used by Höflich (1988) to describe the effect of macroscopic velocity fields in spherical CE of Be stars with detailed non-LTE radiative transfer calculations, which simultaneously reproduce the correct emissions in the Hα, Hβ and Hγ lines and in the visible continuum. Finally, let us note that the line profiles obtained from (9) to (15) can be fitted by a series of three Gaussian functions as done by Andrillat & Fehrenbach (1982) for the Hα emission line. This might perhaps give a marginal justification to the use of (15) as the physics of the Hγ line emission are the same as for the Hα line.

5.4.2. Model Hγ line emission profiles

Some examples of Hγ line emission profiles obtained using relations from (9) to (15) are shown in Fig. 12.

The parameters used in this figure are defined as follows: $\gamma = [(R_e/R_*)^2\Lambda - 1](S_l/F_o^*)$ and $\tau_o = (\sqrt{\pi}e^2/mc^2)\lambda_{H\gamma} f N_T/\Delta_D)$. Figure 12a shows profiles obtained for a set $(\Delta_D, \gamma, \tau_o)$ and several values of S_l/F_o^*. It sketches line profiles suitable for a "Be" phase. Figure 12b is drawn for a set $(\Delta_D, \gamma, S_l/F_o^*)$ and several values of τ_o depicting line profiles likely to be seen in "Be-shell" phases. The line profiles shown in Figs. 12c and d were obtained using relations (9) and (11) which are suited only for the emission peaks and line wings, and they are used for the same sets of $(V_e, \tau_p, R_e, S_l/F_o^*, i)$ values, but for different ellipticities E to depict the sensitivity of our line profiles representation to the flattening of CE and to the inclination angle i. Fits of two observed Hγ line emission profiles and the corresponding fitting parameters are shown in Figs. 12e and f.

The behaviour of line profiles in Fig. 12 can be understood easily. Let us reduce (9) to the form:

$$F_\lambda/F_\lambda^* \simeq e^{-\tau_\lambda} + \Gamma[1 - f(\tau_\lambda)] \quad (16)$$

where the meaning of Γ is similar to γ defined above; $\tau_\lambda = \tau_o e^{-(\Delta\lambda/\Delta\lambda_D)^2}$; $f(\tau_\lambda)$ accounts for the exponentials in (10) and (11). It can readily be shown (Cidale & Ringuelet 1989) that the intensity of the emission peaks depends on the value of Γ and it is independent of the local absorption line profile as well as of the value of τ_o. The maximum of intensity in the emission peaks corresponds to an optical depth $\tau_M = \tau_o\phi(\Delta\lambda_M)$, which is also entirely determined by the value of Γ. Keeping in mind that in our representation (15) the entire macroscopic kinematic effects on the line profile are accounted by Δ_D, for a given value of Γ, the separation of the emission peaks still depends on the value of τ_o. So, the higher the value of τ_o the greater the separation of emission peaks. Figures 8a and b undoubtedly imply that the separation of the emission peaks and the global line broadening have a strong kinematic component due to Keplerian-like movements in the CE. As we have just noticed, there may also be a broadening due to an optical depth effect. It is then interesting to investigate whether some optical depth effect can be detected from observations. The optical depth dependent broadening could give an explanation for the wide scattering seen in Figs. 8a and 8b, which can hardly be attributed only to kinematic effects. This is explored in the following sections.

5.5. Model parameters of the Hγ line emission formation region

All observed Hγ line profiles with emission components were analyzed using the analytical line profiles presented in the preceding section. When the observed emission line profiles were asymmetric we reduced them to equivalent symmetric ones. This was done by averaging the original profiles with their mirror-reflected images and by renormalizing them, so as to preserve the equivalent widths. The fitting parameters obtained: τ_o, Δ_D, S_l/F_o^* and $(R_e/R_*)\Lambda^{1/2}$ are given in Table 7.

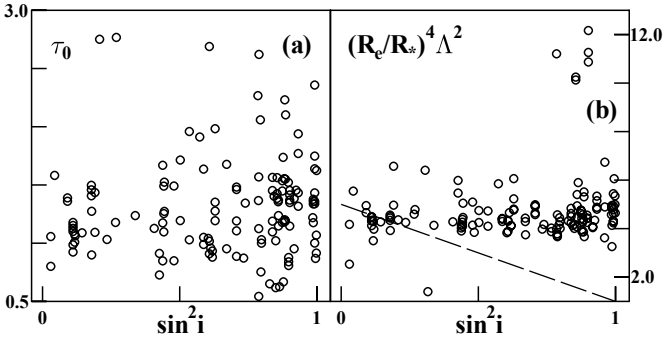

Fig. 13. Optical depth τ_o and $(R_e/R_*)^4\Lambda^2$ against $\sin^2 i$.

5.5.1. Extent, flattening and density distribution in the formation region

To make easier the presentation of further relations between observed and model-dependent quantities, we show in Figs. 13a and b the dependence of τ_o and $(R_e/R_*)^4\Lambda^2$ with $\sin^2 i$, where the aspect angle i was obtained in Sect. 5.1. We have chosen to plot $(R_e/R_*)^4\Lambda^2$ because of its linear dependence with $\sin^2 i$ [relation (12)]. From Fig. 13a it is apparent that the higher values of τ_o are more frequent at $i \to \pi/2$. Rebinning the optical depth τ_o of Fig. 13 as we did for data in Fig. 11, the mean values and the respective 1σ dispersions are:

$\Delta\cos i$	=	1.0–0.8	0.8–0.6	0.6–0.4	0.4–0.2	0.2–0.0
$\overline{\tau_o}$	=	1.146	1.241	1.245	1.327	1.364
σ_τ	=	0.247	0.344	0.411	0.358	0.354

Using (12) and (13) to fit $\overline{\tau_o}$ we obtain $\overline{\tau_p} = 1.13$ and $E = 0.84$. The upper limit of the τ_o distribution against $\sin^2 i$ in Fig. 13a corresponds to $\overline{\tau_p} = 1.50$ and $E = 0.60$. So, both E estimates imply rather modest mean flattenings.

On the other hand, Fig. 13b shows that, except for some rare cases, there is no detected dependence of $(R_e/R_*)^4\Lambda^2$ with the aspect angle. In Fig. 13b we also show the slope over which the results should be distributed if at least a small ellipticity $E = (R_*/R_e)\Lambda^{-1/2}$ could be attributed to the Hγ line emission component formation region. From the values $E \simeq 0.8$ or 1.0, it follows that the average equivalent extent parameter of the Hγ emission line formation region is $\overline{(R_e/R_*)\Lambda^{1/2}} \simeq 1.5 \pm 0.3$. Thus, from $\overline{(R_e/R_*)} \simeq 1.5 \pm 0.3$ and the relation which gives R_e/R_* as a function of α obtained in Sect. 5.4.1, the index α of the power law, $\rho \sim R^{-\alpha}$, of the density distribution in the Hγ line emission formation region is $\alpha \simeq 2.5^{+2.2}_{-0.6}$.

Once we have obtained the value of α, we can calculate the total extent of the Hγ line emission region. Let us assume that this region is characterized by a constant source function, $S_l \simeq$ const. As the emitted flux in the line is then proportional to $1 - e^{-\tau_o}$, we seek the extent R_f/R_* at which a fraction $p = 99\%$ of the emission was

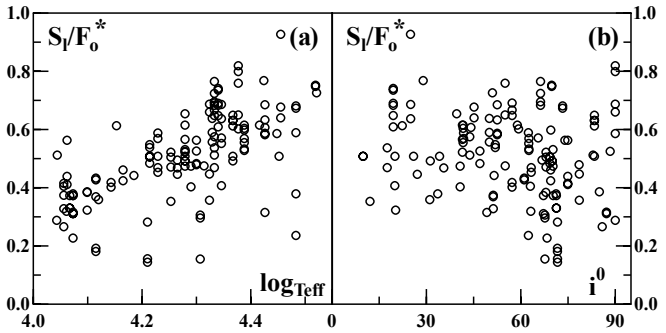

Fig. 14. Source function ratio S_l/F_o^*: **a)** as a function of the effective temperature and **b)** as a function of the aspect angle i.

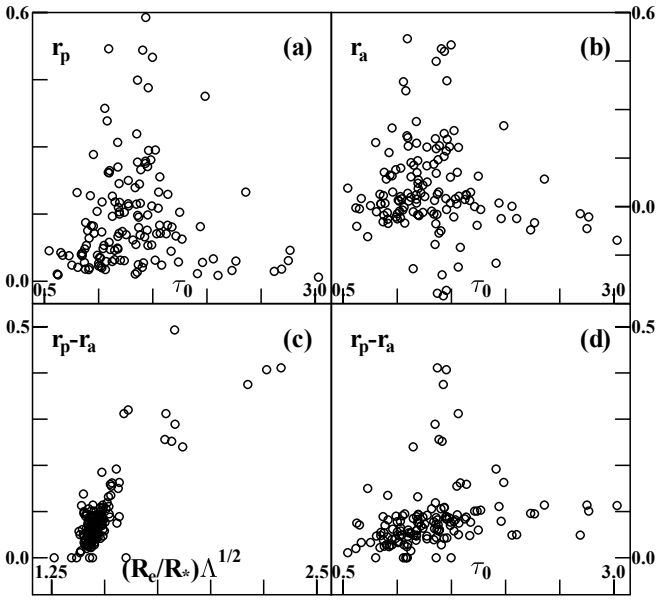

Fig. 15. Residual intensities r_p and r_a against optical depth and extent of the Hγ line emission formation region.

produced. Knowing that $\tau_o \propto N_2$ and $N_2 \propto N_H^2$, where N_H is the column density of hydrogen atoms, we obtain:

$$\frac{R_f}{R_*} = \left\{1 + \frac{\ln[1 - p \times (1 - e^{-\tau_o})]}{\tau_o}\right\}^{\frac{1}{1-2\alpha}}. \quad (17)$$

Having $\alpha = 2.5^{+2.2}_{-0.6}$ and $\tau_o = 1.4^{+1.6}_{-0.9}$, we derive $R_f = 2.6 \pm 1.0 R_*$. As from observation we have $\overline{V \sin i/\Delta_p} = 2.6 \pm 1.0$, values in (5) imply that Huang's (1972) relation overestimates the Hγ line emission formation region by about 40% on average. We shall see in Sect. 5.7 that this is due to the fact that the emission peak separation Δ_p is also a function of the optical depth τ_o.

5.5.2. Density differences according to the latitude

From the fact that R_e/R_* apparently shows no aspect angle dependence, the observed tendency of τ_o values being higher for $i \to \pi/2$ would then imply that gas density increases from the polar towards the equatorial regions. The markedly triangular distribution of points in Fig. 13a from $i \sim 0$ to $i \sim \pi/2$ suggests that the expected mean maximum density contrast in the hydrogen Balmer level population is on average at most $N_2(\text{equator})/N_2(\text{pole}) \sim \tau_o(i \sim \pi/2)/\tau_o(i \sim 0) \sim 2.5/0.5$.

The interpretation of spectroscopic and interferometric data on the Hα and Hβ emission lines in γ Cas with Sobolev radiation transfer calculations and parametrized latitudinal viscosity in the CE implies however that the density contrast is $N_2(\text{equator})/N_2(\text{pole}) \sim 10^2$ and even higher (Stee et al. 1995). Our simple line emission formation representation does not allow us to discuss further details on the value of polar/equator density contrast in the CE. However, as this representation deals with averaged quantities and/or integrated values, such as the optical depth, it would be able to detect systematic higher contrast factors than found here, if they really existed.

5.5.3. The source function

Figure 14a shows the values found for the ratio involving the source function S_l/F_o^* against the effective temperature. Despite some points which deviate from the main trend, there is a rather well-defined mean relation $S_l/F_o^* \simeq -3.03 + 0.83 \times \log T_{\text{eff}}$ which may perhaps partially account for the possibility of higher emission intensities observed in the hotter Be stars (Fig. 9b). Figure 14b shows S_l/F_o^* as a function of the aspect angle i. Except for a few points between $i = 60^o$ and 75^o, most of them are in the $0.5 \lesssim S_l/F_o^* \lesssim 0.8$ interval showing no aspect angle effect. We note that the amount of points in a given inclination (i_1, i_2) interval is [proportional to $|\cos i_1 - \cos i_2|$, which is a consequence of random orientation of stellar rotational axes. The higher number of points at higher values of i together with a small number of points with $S_l/F_o^* \lesssim 0.3$ produces an apparent aspect angle effect, which does not actually exist. As before, the mean values of S_l/F_o^* per $\Delta \cos i$-bins and the respective 1σ dispersions are:

$\Delta \cos i$	=	1.0–0.8	0.8–0.6	0.6–0.4	0.4–0.2	0.2–0.0
$\overline{S_l/F_o^*}$	=	0.610	0.548	0.551	0.425	0.523
σ_{S_l/F_o^*}	=	0.205	0.101	0.134	0.153	0.162

According to Student's test, the deviation of $\overline{S_l/F_o^*}$ in the first $\Delta \cos i$-bin from the global mean value is significant to less than 40%. Due to an increased $\sec i$-dependent optical depth in disc-shaped CE, the value of $\overline{S_l/F_o^*}$ should decrease at $i \to \pi/2$ systematically, because only CE layers with lower temperature do contribute to the radiation seen by the observer. However, in Fig. 14b a such strong i-angle effect is not apparent. Hence, we conclude that the Hγ line emission formation region is probably not too flattened.

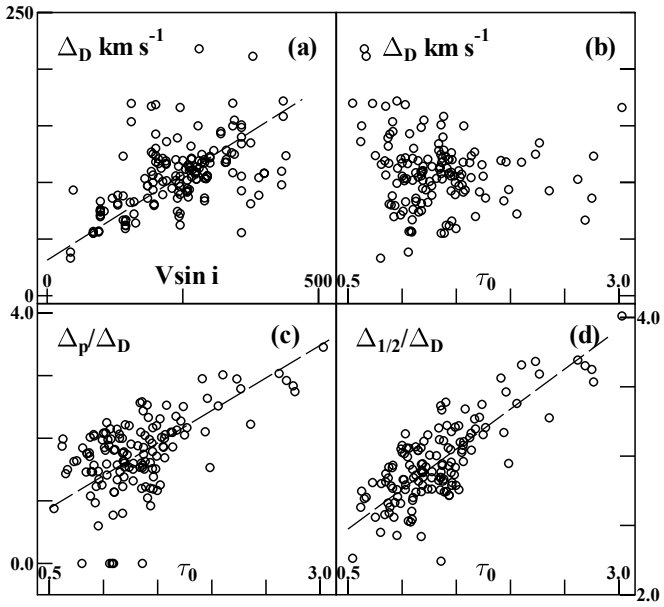

Fig. 16. Total Doppler width Δ_D against: **a)** the $V \sin i$; **b)** the optical depth τ_o at the centre of the Hγ line. Widths Δ_p and $\Delta_{1/2}$ normalized to Δ_D against τ_o, respectively **c)** and **d)**.

5.6. Residual intensities r_p and r_a as a function of the opacity and extent of the Hγ line emission formation region

There is a close linear relation between the equivalent width of the Hγ line emission component and the mean residual intensity in the peaks. So, we present only results that concern the r_p and r_a residual intensities. Figures 15a and 15b show r_p and r_a as functions of τ_o. The triangular distribution in both panels suggests there is an optical depth $\tau_o \sim 1.4$ at which the CE emission seems to be the most effective. From $\tau_o \sim 0.5$ to $\tau_o \sim 1.4$ the emission term $\mathcal{E}$ in (9) dominates, while for $\tau_o \gtrsim 1.4$ the self absorption in the line tends to reduce the total emission. From the discussion in Sect. 5.5.2, it is then apparent that the self absorption is more effective when the star+CE system is seen equator-on.

From the fact that $\overline{R_e \Lambda^{1/2}/R_*} = 1.5$ with quite a low dispersion, the most effective emission is for $\tau_o \sim 1.4$ and the correlation of S_l/F_o^* with T_{eff}, follows the explanation to the upper limit of the emission intensity in the Hγ line as a function of the effective temperature found in Sect. 4.2.

The last behaviour worth noting concerns the depth of the central absorption-like reversal $r_p - r_a$ as a function of $(R_e/R_*)\Lambda^{1/2}$ and of τ_o. They are shown respectively in Figs. 15c and d. No detectable trends are found however for r_p and r_a as functions of $(R_e/R_*)\Lambda^{1/2}$ and τ_o taken separately.

5.7. Dependence of the emission line widths on optical depth

Figure 16a shows the relation between the velocity parameter Δ_D and the $V \sin i$. This relation shows that Δ_D is influenced by a rotational velocity field related to the underlying stellar rotation. Figure 16b shows that there is no relation between Δ_D and the optical depth of the line formation region. The kinematic effects on the line widths Δ_p and $\Delta_{1/2}$ can then be removed by dividing them with Δ_D. Figures 16c and d show that the normalized line widths have a clear dependence on optical depth, as expected from the discussion in Sect. 5.4.2. The rather large spread of the Δ_p/Δ_D and $\Delta_{1/2}/\Delta_D$ against τ_o relations can account for the scatter seen in Figs. 8a and b. Because of the fact that there is a relation between Δ_p/Δ_D and τ_o, it is clear that the simple Huang's (1972) extent parameter, deduced from kinematic grounds, cannot reflect the actual dimension of the Hγ emission line formation region. This also means that no argument on the geometry of this region based on the value of Huang's parameter is reliable, unless the optical depth of the region be negligible. This result was previously foreseen by Hummel (1994) from detailed 3D radiative line transfer calculations in flattened discs.

6. Concluding comments

Three scenarios are most frequently evoked to produce CE in Be stars. They all appeal to rotation and radiation pressure as the main driving forces of the mass lost by the star: ejection of matter by critical rotators (Struve 1931; Limber 1964, 1967; Marlborough 1987); wind-compressed disc model (Bjorkmann & Cassinelli 1993); rotation induced bi-stability model (Lamers & Cassinelli 1999). In all these cases a more or less disc-like CE is produced. Basing their arguments on the spectrophotometric behaviour of Be stars (Moujtahid et al. 1998, 1999) and on their short and long-lived outbursts (Hubert & Floquet 1998; Hubert et al. 2000), Zorec et al. (2000) have suggested that the CE may result from sporadic massive ejections and mass-loaded winds. According to this scenario, the CE would rather have quite an irregular structure with massive clumps moving all around the star. As the mass-loaded winds are produced by the interaction of stellar winds with the surrounding clouds, it can perhaps shape on average, to some degree flattened CE, if wind-compressing and/or bi-stability components act effectively. Therefore, to decide which of these scenarios provides the most reliable explanation of CE formation in Be stars, it makes sense to seek for aspect angle dependence of observed quantities and model-derived parameters. In the present paper, no measured quantity on the observed Hγ line emission profile was found to be i-dependent. Among the model-derived parameters, only τ_o shows some i-dependence, from which we obtained an indication for some pole/equator density contrast in the CE near the star. The optical depth τ_o has been obtained, however, by hiding the whole velocity field in the CE

and its z-dependent density structure in a single effective Doppler width $\Delta\lambda_{\rm D}$ (or velocity parameter $\Delta_{\rm D}$). In order to remove possible ambiguities affecting the estimation of $\tau_{\rm o}$ and consequently also the derivation of column densities and their i-dependence, the velocity components related to the rotation and expansion/contraction of the CE will be explicitly taken into account in a forthcoming paper.

7. Summary and conclusions

We have presented the results of a 10 year observation period of 116 Be stars. Our observations cover the spectral regions containing the He I 4471 and Hγ lines.

$V \sin i$ determinations were derived from the observed He I 4471 line profiles, through comparison with non-LTE, full limb-darkened model line profiles interpolated from the grid by Soeckley & Mihalas (1973). He I 4471 is one of the photospheric lines less affected by emissions or absorptions arising in the CE. The $V \sin i$ values derived for the studied stars are in agreement with those derived by Slettebak (1982) within a dispersion $\sigma \lesssim 30$ km s^{-1} and no systematic deviation. They can be considered as obtained in the new Slettebak's et al. (1975) system. There are 13 discrepant cases where the differences in the $V \sin i$ values cannot be attributed to the method used. In some stars they could be explained in terms of a possible binarity.

We have also presented measurements of different parameters (such as full width at half intensity $\Delta_{1/2}$, separation of double emission peaks $\Delta_{\rm p}$, and equivalent widths W) measured on the emission and absorption components of the observed lines.

Some correlations involving the measured quantities in the Hγ line are analyzed. The observed trend of increasing Δ_p and $\Delta_{1/2}$ with increasing $V \sin i$ is generally interpreted as indicative of rotationally supported CE, which would also be flattened with increased density towards the equatorial plane. However, recent calculations based on kinetic theory of inviscid gaseous envelopes (Rohrmann 1997) do not support the need for a flat envelope in order to explain the observations.

From aspect angle estimations and the relations of Chandrasekhar & Münch (1950) between the projected and true rotational velocities we found that all studied Be stars rotate at nearly the same ratio $V/V_{\rm c}$. From the measured $V \sin i$ and the theoretical distribution of $V \sin i/V_{\rm c}$ for randomly oriented rotational axes, we found the most probable value of $\overline{\omega}$ to be 0.795, thus confirming the earlier results by Moujtahid et al. (1999). We were consequently able to derive the most probable individual values of the angle i for each observed star.

Analysis of the emission intensity in the Hγ line shows no systematic dependence of it nor of the central superimposed absorption on the angle i. We interpret this as further evidence that the regions where the Hγ emission arises are not strongly flattened.

Through modelling of the Hγ emission line profiles we derived estimates of the optical depth for this line. Considering the equivalent width of the Hγ line emission as a function of the optical depth, we find a value of $\tau_{\rm o} \sim 1.4$ for which the CE emission is the most effective, while for larger optical depths the self absorption in the line tends to reduce the total emission. From this fact, the low dispersion of $R_{\rm e}\Lambda^{1/2}/R_*$ around a mean value and the strong correlation of the mean Hγ line source function with the effective temperature, there is a maximum limit to the emission in this line as a function of $T_{\rm eff}$.

Our modelling of the Hγ line profiles was also used to look for the extent, density distribution and changes with latitude in the line emission formation region. We found that the extent of the Hγ line emission formation region in the studied stars is on average $R_{\rm f} \simeq 2.6 \pm 1.0 R_*$. If a power law, $\rho \propto R^{-\alpha}$ is used, the density distribution near the star will be characterized by $\alpha \simeq 2.5^{+2.2}_{-0.6}$. We found that the equator/polar density contrast in the Hγ line emission formation region is about a factor 5, so, one to two orders of magnitude lower than predicted by models with a priori flattened disc-shaped CE. We also found that there is a correlation between the optical depth and the separation of the emission peaks. As a consequence, the simple Huang's (1972) relation produces overestimated values of the Hγ line emission formation region by about 40% on average. As the remaining Balmer line emissions respond to the same physical phenomena as Hγ, the same conclusion should also be extended to them.

Acknowledgements. D. B., L. C. and N. M. acknowledge use at CASLEO of the CCD and data acquisition system supported under U.S. NSF grant AST-90-15827 to R. M. Rich and wish to thank the directors and staff of CASLEO and OHP for the use of their facilities and kind hospitality during the observation runs. We thank an anonymous referee for his her useful comments.

References

Andrillat, Y. 1983, A&AS, 53, 319
Andrillat, Y., & Fehrenbach, C. 1982, A&AS, 48, 93
Andrillat, Y., Jaschek, M., & Jaschek, C. 1990, A&AS, 84, 11
Ballereau, D., Chauville, J., & Zorec, J. 1995, A&AS, 111, 423
Balona, L. A., Henrichs, H. F., & Le Contel, J. M. (eds.) 1994, Pulsation, Rotation and Mass Loss in Early-Type Stars, IAU Symp. 162 (Kluwer Acad. Publ.)
Bjorkmann, J. E., & Cassinelli, J. P. 1993, ApJ, 409, 429
Bodenheimer, P. 1971, ApJ, 167, 153
Brown, A. G. A., & Verschueren, W. 1997, A&A, 319, 811
Chalonge, D., & Divan, L. 1973, A&A, 23, 69
Chandrasekhar, S., & Münch, G. 1950, ApJ, 111, 142
Cidale, L. S., & Ringuelet, A. E. 1989, PASP, 101, 417
Clement, M. 1979, ApJ, 230, 230
Collins II, G. W., & Truax, R. 1995, ApJ, 439, 860
Dachs, J., Hanuschik, R., Kaiser, D., et al. 1986, A&AS, 63, 87
Dachs, J., Hummel, W., & Hanuschik, R. 1992, A&AS, 95, 437
Divan, L., & Zorec, J. 1982, ESA-SP, 177, 101
Floquet, M., Hubert, A. M., Hirata, R., et al. 2000, A&A, 362, 1020
Gillet, D., Burnage, R., Kohler, D., et al. 1994, A&AS, 108, 181
Halbedel, E. M. 1996, PASP, 108, 833

Hanuschik, R. W. 1988, A&A, 190, 187
Hanuschik, R. W. 1989, Ap&SS, 161, 61
Hanuschik, R. W. 1995, A&A, 295, 424
Hanuschik, R. W., Hummel, W., Sutorius, E., et al. 1996, A&AS, 116, 309
Hanuschik, R. W., Kozok, J. R., & Kaiser, D. 1988, A&A, 189, 147
Harmanec, P. 2000, in The Be Phenomenon in Early-Type Stars, IAU Coll., 175, ed. M. A. Smith, H. F. Henrichs, & J. Fabregat, ASP Conf. Ser., 214, 13
Hoffleit, D., & Jaschek, C. 1982, The Bright Star Catalogue – Fourth revised edition, Yale Univeristy Observatory
Höflich, P. 1988, A&A, 191, 348
Horn, K., & Marsh, T. R. 1986, MNRAS, 218, 761
Huang, S. S. 1972, ApJ, 171, 549
Huang, S. S., & Struve, O. 1953, ApJ, 118, 463
Hubert, A. M., & Floquet, M. 1998, A&A, 335, 565
Hubert, A. M., Floquet, M., & Zorec, J. 2000, in The Be Phenomenon in Early-Type Stars, IAU Coll., 175, ed. M. A. Smith, H. F. Henrichs, & J. Fabregat, ASP Conf. Ser., 214, 348
Hubert, A. M., & Hubert, H. 1979, An Atlas of Be Stars, Paris-Meudon Observatory
Hummel, W. 1994, A&A, 289, 458
Hummel, W., & Vrancken, M. 2000, in The Be Phenomenon in Early-Type Stars, IAU Coll., 175, ed. M. A. Smith, H. F. Henrichs, & J. Fabregat, ASP Conf. Ser., 214, 527
Jaschek, M., & Groth, H. G. 1982, Be Stars, IAU Symp., 98 (Reidel, Dordrecht)
Jaschek, M., Slettebak, A., & Jaschek, C. 1981, Be Stars Newsl. No. 4, 9
Koubský, P., Harmanec, P., Hubert, A. M., et al. 2000, A&A, 356, 913
Kurucz, R. L. 1994, Model Atmospheres, CDROM, SAO
Lamers, H. J. G. L. M., & Cassinelli, J. P. 1999, Introduction to Stellar Winds (Cambridge Univ. Press)
Limber, D. N. 1964, ApJ, 140, 139
Limber, D. N. 1967, ApJ, 148, 141
Lyubimkov, L. S. 1996, Ap&SS, 243, 329
Lyubimkov, L. S. 1998, Astr. Rep., 42, 53
Marlborough, J. M. 1987, in Physics of Be Stars, IAU Coll., 92 (Cambridge Univ. Press), 335
Mennickent, R. E., Vogt, N., Barrera, L. H., et al. 1994, A&AS, 106, 427
Mihalas, D. 1972, Non-LTE Model Atmospheres for B and O Stars, NCAR-TN/STR-76, Boulder, Colorado
Moujtahid, A. 1998, Ph.D. Thesis, University Paris VI
Moujtahid, A., Zorec, L., Hubert, A. M., et al. 1998, A&AS, 129, 289
Moujtahid, A., Zorec, L., & Hubert, A. M. 1999, A&A, 349, 151
Porter, J. M. 1996, MNRAS, 280, L31
Rivinius, T., & Štefl, S. 2000, in The Be Phenomenon in Early-Type Stars, IAU Coll. 175, ed. M. A. Smith, H. F. Henrichs, & J. Fabregat, ASP Conf. Ser., 214, 581
Rohrmann, R. D. 1997, MNRAS, 285, 427
Rohrmann, R. D. 2000, Ph.D., University of Córdoba, Argentina
Sackmann, I. J., & Anand, S. P. S. 1970, ApJ, 162, 105
Schaller, G., Schaerer, D., Meynet, G., et al. 1992, A&AS, 96, 269
Slettebak, A. 1976, Be Stars and Shell Stars, IAU Symp., 70 (Reidel, Dordrecht)
Slettebak, A. 1982, ApJS, 50, 55
Slettebak, A., Collins II, G. W., Boyce, P. B., et al. 1975, ApJS, 29, 137
Slettebak, A., Collins II, G. W., & Truax, R. 1992, ApJS, 81, 335
Slettebak, A., & Reynolds, R. C. 1978, ApJS, 38, 205
Slettebak, A., Snow, Th. 1987, Physics of Be Stars, IAU Coll., 92 (Cambridge Univ. Press)
Smith, M. A., Henrichs, H. F., & Fabregat, J. (eds.) 2000, in The Be Phenomenon in Early-Type Stars, IAU Coll., 175, ASP Conf. Ser., 214
Smith, M. A., Hubený, I., & Lanz, T. 1994, in Pulsation, Rotation and Mass Loss in Early-Type Stars, IAU Symp., 162, ed. L. A. Balona, H. F. Henrichs, & J. M. Le Contel, 273
Stee, Ph., & Araújo, F. X. 1994, A&A, 292, 221
Stee, Ph., Araújo, F. X., Vakili, F., et al. 1995, A&A, 300, 219
Steele, I. A. 1999, A&A, 343, 237
Steele, I. A., Negueruela, I., & Clark, J. S. 1999, A&AS, 137, 147
Struve, O. 1931, ApJ, 73, 94
Stoeckley, T. R., & Mihalas, D. 1973, Limb Darkening and Rotation Broadening of Neutral Helium and Ionized Magnesium Line Profiles in Early-Type Stars NCAR-TN/STR 84, Boulder, Colorado
Tarasov, A. E., & Tuominen, I. 1987, in 10th European Regional Meeting of the IAU, 5, 127
Uesugi, A., & Fukuda, I. 1982, Revised Catalogue of Stellar Rotational Velocities, Dep. Astron. Kyoto University
Yang, S., Ninkov, Z., & Walker, G. A. H. 1988, PASP, 100, 233
Yudin, R. V. 2001, A&A, 368, 912
von Zeipel, H. 1924, MNRAS, 84, 665
Zorec, J. 1981, in Effects of Mass-Loss on Stellar Evolution, IAU Coll., 59, ed. C. Chiosi, & R. Stalio (Reidel Publ. Comp.), 539
Zorec, J., & Briot, D. 1991, A&A, 245, 150
Zorec, J., Hubert, A. M., & Moujtahid, A. 2000, in The Be Phenomenon in Early-Type Stars, IAU Coll., 175, ed. M. A. Smith, & H. F. Henrichs, J. Fabregat, ASP Conf. Ser., 214, 448
Zorec, J., Mochkovitch, R., & Divan, L. 1988, C.R. Acad. Paris, 306, 1265
Zorec, J., Mochkovitch, R., & Garcia, A. 1990, in Angular Momentum and Mass Loss for Hot Stars, ed. L. A. Willson, & R. Stalio, NATO ASI Ser., 316, 239
Zorec, J., Israelian, G., Ballereau, D., et al. 1996, A&A, 308, 852

Table 1. The program Be stars and the log of observations.

HD	Name	V mag	Sp.T.	$\log T_{\rm eff}$	$\log g$	Date	HJD $-2\,400\,000$	lines		Obs.
144	10 Cas	5.59	B9IIIe	4.044	3.48	920907	48 872.565	Hγ		OHP
						920907	48 872.601		He I	OHP
4180	o Cas	4.54	B5-6IIIe [a]	4.138	3.43	920903	48 868.595	Hγ		OHP
						920904	48 869.582		He I	OHP
5394	γ Cas	2.47	O9Ve [a]	4.519	3.88	920905	48 870.537	Hγ		OHP
						920907	48 872.616		He I	OHP
						990916	51 437.578	Hγ		OHP
						990923	51 444.571		He I	OHP
6811	ϕ And	4.25	B7Ve	4.099	4.01	920903	48 868.611	Hγ		OHP
						920904	48 869.599		He I	OHP
9612		6.58	B9Ve	4.047	4.04	990915	51 437.525	Hγ		OHP
						990917	51 438.547		He I	OHP
10144	α Eri	0.46	B3Vpe	4.279	4.00	910826	48 494.891	Hγ	He I	ESO
10516	ϕ Per	4.07	B0.5IVe [a]	4.448	3.82	920903	48 868.624	Hγ		OHP
						920904	48 869.615		He I	OHP
11606		7.02	B2Vne	4.346	3.98	990926	51 448.513	Hγ		OHP
						990928	51 450.560		He I	OHP
18552		6.11	B8Vne	4.073	3.99	920905	48 870.564	Hγ		OHP
						920907	48 872.635		He I	OHP
19243		6.62	B1Ve	4.426	3.95	990927	51 448.616	Hγ		OHP
						990923	51 445.543		He I	OHP
20336	BK Cam	4.84	B2Ve [a]	4.346	3.98	920903	48 868.638	Hγ		OHP
						920904	48 869.634		He I	OHP
22192	ψ Per	4.23	B4III-IVe [a]	4.210	3.63	920905	48 870.599	Hγ		OHP
						920907	48 872.650		He I	OHP
						950206	49 755.398	Hγ	He I	OHP
						990916	51 437.587	Hγ		OHP
						990921	51 442.633		He I	OHP
22780		5.57	B7Vne	4.099	4.01	920905	48 870.634	Hγ		OHP
						920907	48 872.663		He I	OHP
23016	13 Tau	5.69	B9Vne	4.047	4.04	910828	48 496.854	Hγ	He I	ESO
23302	17 Tau	3.70	B6IIIe	4.115	3.41	910827	48 495.879	Hγ	He I	ESO
23480	23 Tau	4.18	B6IVe [a]	4.115	3.83	910828	48 496.888	Hγ	He I	ESO
						920119	48 640.537	Hγ	He I	ESO
23552		6.14	B8Vne	4.073	3.99	920908	48 873.584	Hγ		OHP
23630	η Tau	2.87	B8IIIe [a]	4.056	3.38	910828	48 496.906	Hγ	He I	ESO
						920119	48 640.547	Hγ	He I	ESO
23862	28 Tau	5.09	B8IV-Ve [a]	4.067	3.93	910827	48 495.906	Hγ	He I	ESO
						920120	48 641.557	Hγ	He I	ESO
						920904	48 869.659		He I	OHP
						920903	48 868.661	Hγ	He I	OHP
						950211	49 760.289		He I	OHP
						950727	49 925.616		He I	OHP
						950906	49 966.577		He I	OHP
						951101	50 022.526		He I	OHP
						960130	50 113.442		He I	OHP
						960219	50 133.320		He I	OHP
						980929	51 085.656		He I	OHP
						990916	51 437.620	Hγ		OHP
						990921	51 442.655		He I	OHP
24534	X Per	6.10	O9IVe [a]	4.521	3.96	990921	51 442.564	Hγ		OHP
						990917	51 438.636		He I	OHP
25940	48 Per	4.04	B4IVe [a]	4.214	3.81	950206	49 755.292	Hγ	He I	OHP
						960131	50 113.518		He I	OHP
						990916	51 437.650	Hγ		OHP
						990923	51 444.595		He I	OHP
28497	DU Eri	5.60	B1.5Vne [a]	4.388	3.97	900203	47 925.583	Hγ	He I	ESO
						910826	48 494.912	Hγ	He I	ESO
						920117	48 638.594	Hγ	He I	ESO
						960921	50 347.753	Hγ	He I	CAS
30076	56 Eri	5.90	B1.5Ve [a]	4.388	3.97	900204	47 926.593	Hγ	He I	ESO
						920118	48 639.561	Hγ	He I	ESO
						960921	50 347.799	Hγ	He I	CAS
32343	11 Cam	5.08	B4Ve [a]	4.229	4.01	950206	49 755.481	Hγ	He I	OHP
33328	λ Eri	4.27	B2III-IVne [a]	4.329	3.70	900204	47 926.630	Hγ	He I	ESO
						920116	48 637.574	Hγ	He I	ESO
						960921	50 347.831	Hγ	He I	CAS
35411	η Ori	3.36	B1V+B2e	4.426	3.95	920116	48 637.644	Hγ	He I	ESO
35439	ψ^1 Ori	4.95	B1.5III-IVpe [a]	4.372	3.72	920119	48 640.581	Hγ	He I	ESO
36576	120 Tau	5.69	B1IVe [a]	4.416	3.82	950206	49 755.383	Hγ	He I	OHP
37202	ζ Tau	3.00	B2IIIpe [a]	4.324	3.57	920119	48 640.560	Hγ	He I	ESO
						920905	48 870.661	Hγ		OHP
						920907	48 872.672		He I	OHP
						921001	48 896.676		He I	OHP
						941112	49 668.695	Hγ		OHP
						950206	49 755.286	Hγ	He I	OHP
						960130	50 113.497		He I	OHP
						990916	51 437.658	Hγ		OHP
						990921	51 442.670		He I	OHP
37490	ω Ori	4.57	B2-3IIIe [b]	4.290	3.55	900203	47 925.622	Hγ	He I	ESO
						920118	48 639.596	Hγ	He I	ESO

Table 1. continued.

HD	Name	V	Sp.T.	$\log T_{\rm eff}$	$\log g$	Date	HJD	lines		Obs.
37795	α Col	2.64	B6IVe [a]	4.115	3.83	920116	48 637.656	Hγ	He I	ESO
41335		5.21	B1.5IIIen [a]	4.367	3.62	900204	47 926.659	Hγ	He I	ESO
						920117	48 638.636	Hγ	He I	ESO
						920120	48 641.661	Hγ	He I	ESO
						950206	49 755.353	Hγ	He I	OHP
						960306	50 148.555	Hγ	He I	CAS
44458	FR CMa	5.64	B0.5Vpe [a]	4.455	3.94	900202	47 924.646	Hγ	He I	ESO
						920118	48 639.666	Hγ	He I	ESO
45725	β Mon	4.60	B2.5IV-Ve [b]	4.307	3.91	900206	47 928.547	Hγ	He I	ESO
						920116	48 637.686	Hγ	He I	ESO
						960308	50 150.671	Hγ	He I	CAS
45995		6.14	B1.5IVnne [a]	4.377	3.82	950206	49 755.415	Hγ	He I	OHP
47054		5.52	B8IV-Ve [b]	4.067	3.93	900204	47 926.710	Hγ	He I	ESO
						920118	48 639.705	Hγ	He I	ESO
						960308	50 150.686	Hγ	He I	CAS
48917	10 CMa	5.20	B2III-IVe [a]	4.329	3.70	900203	47 925.653	Hγ	He I	ESO
						920119	48 640.674	Hγ	He I	ESO
						960308	50 150.704	Hγ	He I	CAS
50013	κ CMa	3.96	B1.5IVne [b]	4.377	3.82	900202	47 924.593	Hγ	He I	ESO
						920115	48 636.637	Hγ	He I	ESO
54309	FV CMa	5.71	B2IVe [b]	4.333	3.81	900206	47 928.604	Hγ	He I	ESO
						920115	48 636.674	Hγ	He I	ESO
56014	27 CMa	4.66	B3IIIe [a]	4.253	3.54	920120	48 641.693	Hγ	He I	ESO
						960308	50 150.724	Hγ	He I	CAS
56139	ω CMa	3.85	B2IVe [a]	4.333	3.81	900203	47 925.686	Hγ	He I	ESO
						920115	48 636.711	Hγ	He I	ESO
57219	NW Pup	5.11	B2IVne [b]	4.333	3.81	900206	47 928.639	Hγ	He I	ESO
						920119	48 640.746	Hγ	He I	ESO
58050	OT Gem	6.41	B2Ve [a]	4.346	3.98	950206	49 755.461	Hγ	He I	OHP
						960220	50 134.478		He I	OHP
						960221	50 135.430	Hγ		OHP
58343	FW CMa	5.33	B4IVe [a]	4.214	3.81	900204	47 926.749	Hγ	He I	ESO
						920119	48 640.712	Hγ	He I	ESO
58978	FY CMa	5.61	B0Vpe [a]	4.483	3.92	900206	47 928.673	Hγ	He I	ESO
						920117	48 638.702	Hγ	He I	ESO
60606	OW Pup	5.54	B3Vne [b]	4.279	4.00	900206	47 928.717	Hγ	He I	ESO
						920120	48 641.725	Hγ	He I	ESO
63462	o Pup	4.50	B0Ve [a]	4.483	3.92	900202	47 924.698	Hγ	He I	ESO
						920116	48 637.728	Hγ	He I	ESO
66194	V374 Car	5.81	B2.5IVe [c]	4.300	3.82	900207	47 929.627	Hγ	He I	ESO
						920120	48 641.749	Hγ	He I	ESO
68980	MX Pup	4.78	B0.5IV-Ve [a]	4.452	3.88	900203	47 925.713	Hγ	He I	ESO
						920115	48 636.741	Hγ	He I	ESO
75311	V344 Car	4.49	B2.5IVne [b]	4.300	3.82	900203	47 925.737	Hγ	He I	ESO
						920117	48 638.742	Hγ	He I	ESO
77320	IU Vel	6.07	B3Vne [b]	4.279	4.00	900207	47 929.693	Hγ	He I	ESO
						920118	48 639.742	Hγ	He I	ESO
83953		4.77	B5IV-Ve [a]	4.165	3.63	900202	47 924.734	Hγ	He I	ESO
						920117	48 638.772	Hγ	He I	ESO
86612		6.21	B4Ve [b]	4.229	4.01	900203	47 925.816	Hγ	He I	ESO
						920115	48 636.793	Hγ	He I	ESO
88661	QY Car	5.72	B2IVpne [b]	4.333	3.81	900206	47 928.775	Hγ	He I	ESO
						920117	48 638.807	Hγ	He I	ESO
						960306	50 148.669	Hγ	He I	CAS
89080	ω Car	3.32	B8IIIe	4.056	3.38	920120	48 641.767	Hγ	He I	ESO
91120		5.58	B9IVne [a]	4.043	3.88	900204	47 926.790	Hγ	He I	ESO
						920118	48 639.782	Hγ	He I	ESO
91465	PP Car	3.32	B3IIIne [a]	4.253	3.54	900202	47 924.754	Hγ	He I	ESO
						920115	48 636.831	Hγ	He I	ESO
						960306	50 148.694	Hγ	He I	CAS
105435	δ Cen	2.60	B2IVne [b]	4.333	3.81	900203	47 925.854	Hγ	He I	ESO
						910827	48 496.474	Hγ	He I	ESO
						920115	48 636.844	Hγ	He I	ESO
						960306	50 148.706	Hγ	He I	CAS
105521	V817 Cen	5.48	B3IVe	4.265	3.82	960306	50 148.726	Hγ	He I	CAS
109387	κ Dra	3.87	B5-6IVpe [a]	4.143	3.84	950207	49 755.565	Hγ		OHP
						960221	50 134.541		He I	OHP
						960221	50 135.474	Hγ		OHP
110432		5.31	B1.5IVe [b]	4.377	3.82	900202	47 924.790	Hγ	He I	ESO
						920118	48 639.812	Hγ	He I	ESO
112078	λ Cru	4.62	B4Vne [b]	4.229	4.01	900207	47 929.858	Hγ	He I	ESO
						910830	48 499.474	Hγ	He I	ESO
						920118	48 639.840	Hγ	He I	ESO
112091	μ^2 Cru	5.17	B5Vne [b]	4.185	4.02	900202	47 924.844	Hγ	He I	ESO
113120		6.03	B2IIIne [b]	4.324	3.57	900207	47 929.737	Hγ	He I	ESO
						920120	48 641.800	Hγ	He I	ESO
120324	μ Cen	3.04	B2IVe [b]	4.333	3.81	900202	47 924.874	Hγ	He I	ESO
						910826	48 495.496	Hγ	He I	ESO
						920115	48 636.853	Hγ	He I	ESO
124367	V795 Cen	5.07	B4IVne [b]	4.214	3.81	900204	47 926.830	Hγ	He I	ESO
						910827	48 496.500	Hγ	He I	ESO

Table 1. continued.

HD	Name	V	Sp.T.	$\log T_{\rm eff}$	$\log g$	Date	HJD	lines		Obs.
						920119	48 640.805	Hγ	He I	ESO
127972	η Cen	2.31	B2IV-Vne [b]	4.340	3.90	900205	47 927.827	Hγ	He I	ESO
						910827	48 495.506	Hγ	He I	ESO
						960308	50 150.839	Hγ	He I	CAS
131492	θ Cir	5.11	B3Vnpe [a]	4.279	4.00	900206	47 928.828	Hγ	He I	ESO
						910828	48 497.487	Hγ	He I	ESO
						920119	48 640.835	Hγ	He I	ESO
134481	κ1 Lup	3.87	B9.5Vne	4.018	2.76	910827	48 495.520	Hγ	He I	ESO
135734	μ Lup	4.27	B8Ve	4.073	3.99	900207	47 929.877	Hγ	He I	ESO
						910828	48 496.534	Hγ	He I	ESO
						920120	48 641.833	Hγ	He I	ESO
137387	κ1 Aps	5.49	B1pne	4.426	3.95	900207	47 929.827	Hγ	He I	ESO
						910829	48 497.532	Hγ	He I	ESO
						920120	48 641.869	Hγ	He I	ESO
138749	θ CrB	4.14	B5Vnne [a]	4.185	4.02	960703	50 268.366		He I	OHP
142184		5.42	B2.5Vne	4.314	3.99	910830	48 498.531	Hγ	He I	ESO
142983	48 Lib	4.88	B3-4III-IVpe [a]	4.235	3.67	900204	47 926.865	Hγ	He I	ESO
						910825	48 494.498	Hγ	He I	ESO
						910831	48 500.511	Hγ	He I	ESO
						920119	48 640.862	Hγ	He I	ESO
148184	χ Oph	4.42	B0.5Vpe [a]	4.455	3.94	900206	47 928.856	Hγ	He I	ESO
						910829	48 497.575	Hγ	He I	ESO
						920118	48 639.860	Hγ	He I	ESO
149757	ζ Oph	2.56	O9Vn [a]	4.519	4.00	900206	47 928.872	Hγ	He I	ESO
						910829	48 497.591	Hγ	He I	ESO
						920120	48 641.852	Hγ	He I	ESO
157042	ι Ara	5.25	B2IVe [b]	4.300	3.82	910830	48 498.578	Hγ	He I	ESO
158427	α Ara	2.95	B3Vne [a]	4.279	4.00	910830	48 498.607	Hγ	He I	ESO
158643	51 Oph	4.81	B9.5Ve	4.018	4.02	910830	48 498.629	Hγ	He I	ESO
164284	66 Oph	4.64	B1Ve [a]	4.426	3.95	910826	48 494.544	Hγ	He I	ESO
						920902	48 868.334	Hγ		OHP
						920903	48 869.314		He I	OHP
						960703	50 268.394		He I	OHP
						960922	50 348.571	Hγ	He I	CAS
						970914	50 705.592	Hγ	He I	CAS
167128		5.33	B3IIIep	4.253	3.54	910829	48 497.621	Hγ	He I	ESO
173948	λ Pav	4.22	B1.5IIIe [a]	4.367	3.62	910826	48 494.576	Hγ	He I	ESO
174237	CX Dra	5.88	B3Ve [a]	4.279	4.00	920904	48 870.313	Hγ		OHP
						920905	48 871.314		He I	OHP
174638	β Lyr	3.45	B7Ve+A8p	4.099	4.01	920906	48 872.287	Hγ		OHP
						920906	48 872.395		He I	OHP
175869	64 Ser	5.57	B9IIIep:Hg:	4.044	3.48	910829	48 497.677	Hγ	He I	ESO
178175	V4024 Sgr	5.54	B2Ve [a]	4.346	3.98	910826	48 494.614	Hγ	He I	ESO
183656	V923 Aql	6.05	B6VeShell [a]	4.139	4.03	910828	48 496.595	Hγ	He I	ESO
						920907	48 873.317	Hγ		OHP
						920907	48 873.384		He I	OHP
183914	β^2 Cyg	5.11	B8Ve	4.073	3.99	920906	48 872.307	Hγ		OHP
						920906	48 872.399		He I	OHP
184279	V1294 Aql	6.82	B0Ve [a]	4.483	3.92	910827	48 495.590	Hγ	He I	ESO
185037	11 Cyg	6.05	B8Vne	4.073	3.99	920904	48 870.355	Hγ		OHP
						920905	48 871.356		He I	OHP
187811	12 Vul	4.95	B2.5Ve [a]	4.314	3.99	920906	48 872.324	Hγ		OHP
						920906	48 872.417		He I	OHP
189687	25 Cyg	5.19	B3IVe	4.265	3.82	920904	48 870.391	Hγ		OHP
						920905	48 871.391		He I	OHP
191610	28 Cyg	4.93	B3IVe [a]	4.265	3.82	920904	48 870.414	Hγ		OHP
						920905	48 871.416		He I	OHP
192044	20 Vul	5.92	B7Ve	4.099	4.01	920906	48 872.357	Hγ		OHP
						920906	48 872.440		He I	OHP
193911	25 Vul	5.54	B8IIIne	4.056	3.38	920907	48 873.353	Hγ		OHP
						920907	48 873.418		He I	OHP
198183	λ Cyg	4.53	B5Ve	4.185	4.02	920907	48 873.435		He I	OHP
						920907	48 873.492	Hγ		OHP
200120	59 Cyg	4.74	B1.5Vne [a]	4.388	3.97	920902	48 868.363	Hγ		OHP
						920903	48 869.344		He I	OHP
201733		6.63	B4IVpe	4.214	3.81	990915	51 437.435	Hγ		OHP
						990916	51 438.458		He I	OHP
202904	υ Cyg	4.43	B3Vne [a]	4.279	4.00	920902	48 868.410	Hγ		OHP
						920903	48 869.400		He I	OHP
203467	6 Cep	5.18	B3IVe	4.265	3.82	920902	48 868.429	Hγ		OHP
						920903	48 869.418		He I	OHP
						940809	49 574.414		He I	OHP
204860		6.90	B5.5Ve	4.162	4.03	990920	51 442.458	Hγ		OHP
205637	ϵ Cap	4.68	B3II-IIIpe [a]	4.238	3.73	910826	48 494.659	Hγ	He I	ESO
						910831	48 499.767	Hγ	He I	ESO
						960921	50 347.635	Hγ	He I	CAS
208057	16 Peg	5.08	B3Ve	4.279	4.00	910828	48 496.683	Hγ	He I	ESO
208682		5.86	B2.5Ve	4.314	3.99	920907	48 873.466		He I	OHP
						920908	48 873.523	Hγ		OHP
209014	*eta* PsA	5.42	B8Ve	4.073	3.99	910826	48 494.700	Hγ	He I	ESO
						910829	48 497.792	Hγ	He I	ESO
209409	*o* Aqr	4.69	B6IVe [a]	4.155	3.83	910827	48 495.662	Hγ	He I	ESO

Table 1. continued.

HD	Name	V	Sp.T.	$\log T_{\rm eff}$	$\log g$	Date	HJD	lines		Obs.
						910830	48 498.667	Hγ	He I	ESO
209522		5.96	B4IVne	4.214	3.81	910827	48 595.768	Hγ	He I	ESO
210129	25 Peg	5.78	B6-7Vne [a]	4.120	4.02	910828	48 496.728	Hγ	He I	ESO
212076	31 Peg	5.01	B2IV-Ve	4.340	3.90	910827	48 495.699	Hγ	He I	ESO
						910831	48 499.814	Hγ	He I	ESO
						920902	48 868.458	Hγ		OHP
						920903	48 869.446		He I	OHP
						920906	48 872.469		He I	OHP
						920907	48 872.520	Hγ		OHP
						960130	50 113.273		He I	OHP
						960921	50 347.635	Hγ	He I	CAS
						970913	50 704.689	Hγ	He I	CAS
212571	π Aqr	4.66	B1Ve [a]	4.426	3.95	910826	48 494.834	Hγ	He I	ESO
214168	8 Lac	5.73	B2Ve	4.346	3.98	920906	48 872.489		He I	OHP
						920907	48 872.541	Hγ		OHP
214748	ϵ PsA	4.17	B8IVe [a]	4.061	3.87	910826	48 494.734	Hγ	He I	ESO
						910829	48 497.828	Hγ	He I	ESO
217050	EW Lac	5.43	B3IIIeshell [a]	4.253	3.54	920904	48 870.482	Hγ		OHP
						920905	48 871.489		He I	OHP
						960130	50 113.351		He I	OHP
217891	β Psc	4.53	B5-6IV-Ve [a]	4.153	3.93	910826	48 494.780	Hγ	He I	ESO
224544		6.52	B6IVe	4.115	3.83	990924	51 446.465	Hγ		OHP
						990928	51 450.446		He I	OHP
224559	LQ And	6.54	B4Ven	4.229	4.01	920903	48 868.564	Hγ		OHP
						920904	48 869.550		He I	OHP
						990926	51 448.429	Hγ		OHP

Note: "a" ≡ BCD classification in Moujtahid et al. (1998), Zorec & Briot (1991); "b" ≡ classification in Ballereau et al. (1995); Date ≡ (year)(month)(day); CAS ≡ CASLEO; ESO ≡ European Southern Observatory; OHP ≡ Observatoire de Haute Provence; Hγ ≡ H I λ4340; He I ≡ He I λ4471.